INFORMATION TO USERS

This manuscript has been reproduced from the microfilm master. UMI films the text directly from the original or copy submitted. Thus, some thesis and dissertation copies are in typewriter face, while others may be from any type of computer printer.

The quality of this reproduction is dependent upon the quality of the copy submitted. Broken or indistinct print, colored or poor quality illustrations and photographs, print bleedthrough, substandard margins, and improper alignment can adversely affect reproduction.

In the unlikely event that the author did not send UMI a complete manuscript and there are missing pages, these will be noted. Also, if unauthorized copyright material had to be removed, a note will indicate the deletion.

Oversize materials (e.g., maps, drawings, charts) are reproduced by sectioning the original, beginning at the upper left-hand corner and continuing from left to right in equal sections with small overlaps. Each original is also photographed in one exposure and is included in reduced form at the back of the book.

Photographs included in the original manuscript have been reproduced xerographically in this copy. Higher quality 6" x 9" black and white photographic prints are available for any photographs or illustrations appearing in this copy for an additional charge. Contact UMI directly to order.

UMI®

Bell & Howell Information and Learning
300 North Zeeb Road, Ann Arbor, MI 48106-1346 USA
800-521-0600

Admittance of an Ionospheric Rocket Antenna

by

Ting-Chung Chu

September 1998

A thesis submitted in conformity with the requirements
for the degree of Master of Applied Science
Department of Electrical and Computer Engineering
University of Toronto

National Library
of Canada

Acquisitions and
Bibliographic Services

395 Wellington Street
Ottawa ON K1A 0N4
Canada

Bibliothèque nationale
du Canada

Acquisitions et
services bibliographiques

395, rue Wellington
Ottawa ON K1A 0N4
Canada

Your file Votre référence

Our file Notre référence

0-612-40936-8

Admittance of an Ionospheric Rocket Antenna

Ting C. Chu

Master of Applied Science
Department of Electrical and Computer Engineering
University of Toronto
1998

ABSTRACT

Considered here is the experimental and theoretical input admittance of a plasma-immersed monopole antenna oriented in the direction perpendicular to the ambient magnetic field. The study is motivated by the need to know the admittance of the antennas used in the OEDIPUS-C ionospheric rocket experiment. Theoretical calculations were carried out by adapting an existing approximate transmission-line analysis. Corresponding scale-model laboratory experiments were carried out in a laboratory plasma chamber. Theory and measurements focused on resonance behaviour caused by sheath waves propagating along the antenna. Theoretically predicted low-frequency sheath-wave passbands are in accordance with experimentally observed resonance characteristics. In particular, the existence of a very-low-attenuation passband above the cyclotron frequency in the presence of a weak ambient magnetic field has been identified.

ACKNOWLEDGEMENTS

I am greatly indebted to the guidance and patience of Prof. K. G. Balmain who has provided ample advice and financial support during the preparation of this thesis. This project would not have been possible without his resourceful insight. I would also like to thank Andrea Lüttgen for sharing her expertise and experience in the subject of the study. Special thanks to Gerald Dubois and Peter Kremer for their contribution to solving the many problems encountered in the design and implementation of laboratory work. Many thanks to colleagues in the Electromagnetics Group: Bengt Littmann, Karam Noujeim, Leesa MacLeod, Kuen-Wei Shieh, Paul Wang, and Xidong Wu for their technical suggestions. I would like to dedicate this work to my late father who had passed away during the preparation of this thesis, and my mother who has given me her time throughout the years to which I am grateful.

TABLE OF CONTENTS

Chapter 1

INTRODUCTION

1.1 Background

When a material object is immersed in a plasma, a negative electric potential is established at its bounding surface relative to the plasma. This is a consequence of high electron mobility as electrons rush to the surface leaving the less mobile ions behind during the first instants of contact. Within a short period of time, the build-up of electrons charges the surface to a negative potential, preventing further electron motion toward the material boundary. As a result, the immediate vicinity of the material surface is depleted of electrons, and therefore is known as the ion sheath. Because of the inability of ions to respond to high frequency electromagnetic excitations, the ion sheath may be considered as a vacuum gap as far as high frequency electromagnetic waves are concerned. The sheath thickness is comparable to a "Debye length", a quantity proportional to the square root of the ratio of the electron temperature to the electron density.

Now suppose that the "material object" is a metal wire. This situation resembles a dielectric (the vacuum gap representing the sheath) bounded by two conductors, a good conductor (the wire) and a poor conductor (the plasma), somewhat analogous to a coaxial transmission line. This analogy suggests that the ion sheath could serve as a waveguide through which electromagnetic waves might propagate with some losses (Balmain [1]). Such "sheath wave" propagation is easy to observe but is strongly influenced by an ambient, steady magnetic field such as the earth's magnetic field which permeates the ionospheric plasma and renders it anisotropic.

The issue of sheath wave propagation has been approached by various authors from both theoretical and experimental perspectives. Previous studies of the propagation phenomenon along a wire were mostly limited to laboratory arrangements in which the orientation of the conductor surface with respect to the ambient magnetic field remains invariant over the dimensions of the conductor. As an example, a theoretical formulation of the sheath wave dispersion relation was presented by Laurin [2] using an anisotropic, cold-plasma, vacuum-gap-sheath approximation with a simplified planar conductor geometry. For wave propagation parallel to the ambient magnetic field, this revealed a low frequency primary passband up to the cyclotron frequency and a secondary higher-attenuation passband from the cyclotron frequency to $\frac{1}{\sqrt{2}}$ times the upper hybrid frequency. Experimental verification of this simplified theoretical analysis was also obtained by Laurin [2] for propagation along a cylindrical wire oriented parallel to the ambient magnetic field. However, the agreement between theory and experiment was only qualitative. Baker [3] established a similar planar plasma-sheath model for propagation normal to the ambient magnetic field and found wave cutoff (stopband) conditions below the cyclotron frequency and a relatively high-attenuation passband between the cyclotron frequency and the upper hybrid frequency divided by $\sqrt{2}$. Existence of the predicted stopband and passband was supported qualitatively by experimental evidence.

1.2 OEDIPUS Experiments

Large-scale testing of the aforementioned theory was implemented by a tether-payload rocket experiment conducted in the ionosphere. The OEDIPUS (Observations of Electric-field Distributions in the Ionospheric Plasma - a Unique Strategy) project was an experiment whose purpose was to observe the phenomenon of propagation of radiated waves and tether-guided sheath waves in the ionospheric plasma (James and Balmain [4], James *et al.* [5]). Specifically, a plane wave propagation experiment was conducted on board the rocket using four-arm dipole antennas located on the two separated rocket sections with nose and tail joined by a tether. In addition, the effect of tethers on electromagnetic coupling via sheath waves was examined by a transmission experiment with a transmitter and a synchronized receiver situated respectively in the nose and tail subpayloads. This is illustrated in Fig. 1-1.

Magnetic-field-parallel propagation characteristics formulated on the premises of cold plasma theory have been confirmed by experimental results of tether-guided signal transmission obtained from the OEDIPUS-A flight. Evidence of weakly attenuated low-frequency wave propagation up to the cyclotron frequency was in accordance with the spectrum of the primary passband as deduced in theory. Implications of these findings with regard to electromagnetic compatibility on plasma-immersed space structures such as the Space Station are believed to be significant: propagation of low-frequency noise via sheath waves could cause interference with

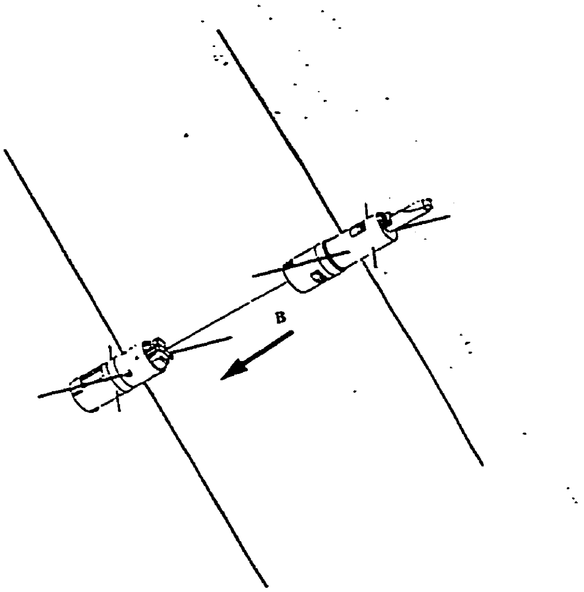

Figure 1-1. Orientation of crossed dipoles on the OEDIPUS-C rocket with respect to the ambient magnetic field.

electrical systems on board (Balmain *et al.* [6]).

1.3 Present Work in Perspective

The present study of sheath wave effects on antenna impedance was proposed for the particular case in which an antenna wire has its axis perpendicular to the magnetic field. Such an arrangement is consistent with the orientation of the dipole antennas in the OEDIPUS-C tethered sounding rocket experiment. The motivations behind this investigation are 1) the lack of understanding of propagation characteristics for this specific geometry in which the near fields have an azimuthal dependence, and 2) the need for antenna impedance estimates to support the interpretation of the OEDIPUS-C results.

Because of the mathematical complexity anticipated in a rigorous field analysis for this arrangement, the proposed study was limited to laboratory work and comparison with results obtained from approximate transmission-line theory. A laboratory experiment was proposed in which two coaxial cable-monopole antenna assemblies are immersed in a magnetoplasma. The antenna of interest was oriented perpendicular to the direction of the ambient magnetic field while the reference antenna which was used for plasma-diagnostic purposes was aligned with the magnetic field. The reflection coefficient from the antenna wires was measured over a linearly swept frequency range from 300 kHz to a few gigahertz. Antenna impedance as a function of frequency was derived from the reflection coefficient measurement, and particular attention was given to resonance phenomena along the monopole antennas. Laboratory results were compared with values obtained from an adaptation of an existing transmission-line theory of input admittance for plasma-immersed antenna structures (Adachi *et al.* [7]).

Chapter 2

TRANSMISSION-LINE THEORY FOR PLASMA-IMMERSED DIPOLES

2.1 Concept of Transmission-Line Theory

Formulation of a transmission-line model for sheathless plasma-immersed dipole antennas was initially implemented by Adachi *et al.* [7], who had suggested that such an analysis is plausible because of the resemblance between the antenna of interest and a transmission line. This analogy is supported in part by the non-radiative characteristic of sheath waves which form a significant subset of the wave modes that can exist along a wire in plasma.

Adachi *et al.* [7] had computed the distributed inductance and capacitance of the antenna by quasi-static methods. These parameters are subsequently incorporated into the general transmission-line theory from which the propagation constant and the characteristic impedance are readily calculated. The impedance of the antenna is then presented utilizing the above parameters for a dipole oriented at an arbitrary angle with respect to the static magnetic field. It is the purpose of the present work to adapt the existing transmission-line formulation by considering the effects of the ion sheath in the form of distributed capacitance, thus modifying the resonance frequencies predicted by Adachi *et al.* [7].

2.2 Geometry of the Proposed Problem

The crossed-dipole antenna on the OEDIPUS-C rocket is treated in theory as two dipoles in parallel as shown in Fig. 2-1. This arrangement of parallel dipoles can be expressed as a thin cylindrical antenna with half length l and radius ρ immersed in an anisotropic cold plasma with

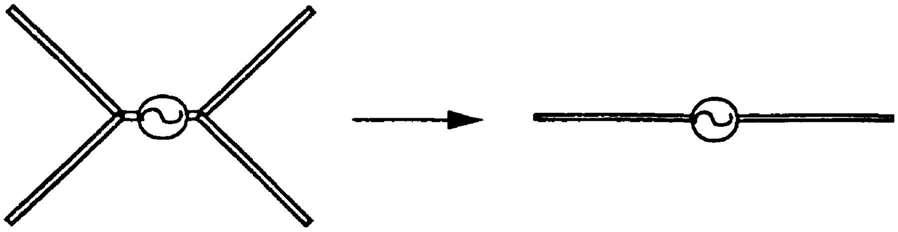

Figure 2-1. OEDIPUS-C crossed dipoles treated as two dipoles in parallel.

an angle of inclination θ between the antenna axis and the static magnetic field. The dielectric tensor for the anisotropic plasma medium is given as

$$\overline{K} = \begin{bmatrix} K' & jK'' & 0 \\ -jK'' & K' & 0 \\ 0 & 0 & K_0 \end{bmatrix}$$

where $K_0 = 1 - \frac{X}{U}$, $K' = 1 - \frac{XU}{U^2 - Y^2}$, $K'' = \frac{-XY}{U^2 - Y^2}$

and $X = \frac{\omega_p{}^2}{\omega^2}$, $Y = \frac{\omega_c}{\omega}$, $U = 1 - j\frac{\nu}{\omega}$

in which ω_p, ω_c, and ν are respectively the plasma, cyclotron and collision frequencies.

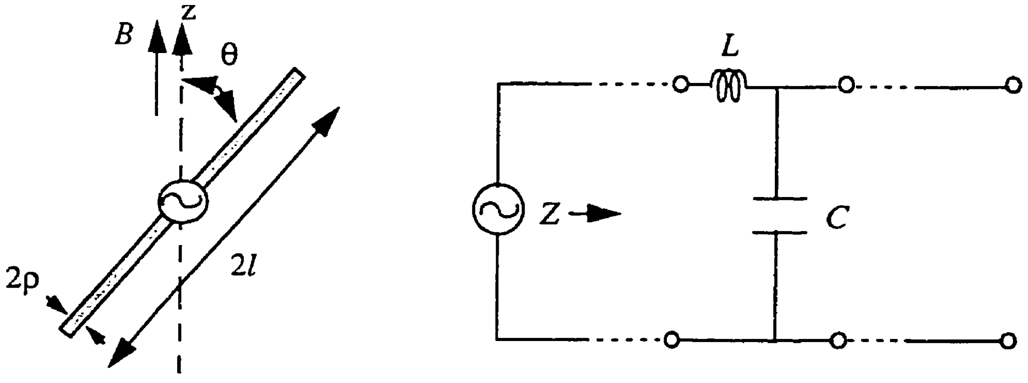

Figure 2-2. Analogy between monopole antenna and transmission line.

2.3 Distributed Inductance of Antenna

The inductance per unit length for the transmission-line model applicable to a monopole is deduced from Adachi [7] and is given by

$$L = \frac{\mu}{2\pi}\left[-1+\log\left(\frac{2l}{\rho}\right)\right] \tag{2-1}$$

2.4 Distributed Capacitance of Antenna

The distributed capacitance for the representation can be derived by regarding the antenna in the plasma as a cylindrical capacitor in which the cylindrical metal antenna is the inner conductor, the ion sheath is the dielectric (modelled as a vacuum gap), and the surrounding anisotropic plasma is the outer conductor. The plasma contribution to the capacitance may be computed by evaluating the electrostatic potential due to a linear charge distribution along the antenna axis, then utilizing the definition of capacitance to obtain the required expression.

Miyazaki [8] had formulated the electrostatic potential due to a line charge in the presence of a static magnetic field. In a situation in which the antenna length is shorter than the propagating wavelength in free space, quasi-static assumption is invoked in which time variation of the vector potential is neglected in comparison with the static component of the electric field. Consequently, the problem is reduced to solving the modified Poisson's equation. It should be noted that the use of the quasi-static conditions is consistent with the assumed uniform current distribution employed in the derivation of distributed antenna inductance as given by eq (2-1).

For a uniform linear charge density of q per unit length, the potential at a point (x, y, z) in rectangular co-ordinates can be written as given by Miyazaki as

$$\psi = \frac{q}{4\pi\varepsilon_0\sqrt{K'K}}\ln\left|\frac{2Kl+K'b+2K'\sqrt{K(Kl^2+bl+c)}}{-2Kl+K'b+2K'\sqrt{K(Kl^2-bl+c)}}\right| \tag{2-2}$$

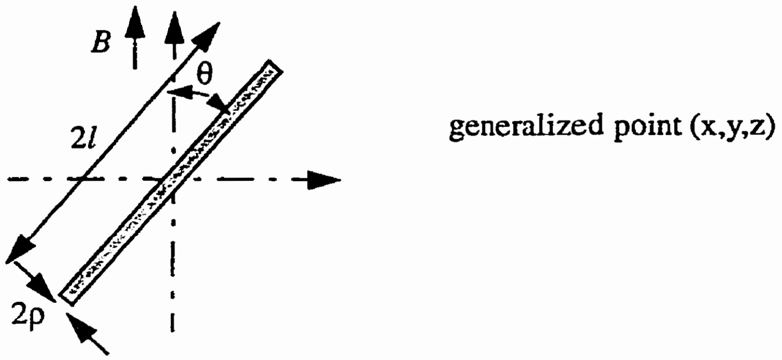

Figure 2-3. Electrostatic potential due to a line charge in a plasma.

where $K = K_0(\sin\theta)^2 + K'(\cos\theta)^2$, $b = -2z\cos\theta - 2\left(\frac{K_0}{K'}\right)y\sin\theta$ and $c = \frac{K_0}{K'}(x^2+y^2)+z^2$

The potential at the sheath-plasma interface with co-ordinates $x = \rho + s, y = 0, z = 0$, while making use of the assumptions that $|K|l^2 \gg 4|K_0|(\rho+s)^2$ and $l \gg \rho + s$, is given by

$$\psi_{\rho+s} = \frac{q}{2\pi\varepsilon_0\sqrt{K'K}}\ln\left(\frac{l}{\rho+s}\right) \tag{2-3}$$

Equation (2-3) describes the potential at the sheath-plasma interface of one conductor relative to the reference value at infinity. Utilizing the definition of capacitance, the distributed capacitance (per unit length) arising from the plasma contribution to the single conductor can be computed as

$$C_p = \frac{q}{\psi_{\rho+s}} = 2\pi\varepsilon_0\sqrt{K'K}\left[\ln\left(\frac{l}{\rho+s}\right)\right]^{-1} \tag{2-4}$$

The distributed capacitance contributed by the vacuum sheath can be found by calculating the quasi-static potential difference between the wire surface and the plasma-sheath interface. Evaluating eq. (2-2) in free space at $x = \rho$ and $x = \rho + s$ yields a potential difference of

$$\Delta\psi = \frac{q}{2\pi\varepsilon_0}\ln\left(\frac{\rho+s}{\rho}\right) \tag{2-5}$$

which leads to the distributed capacitance (per unit length) given by

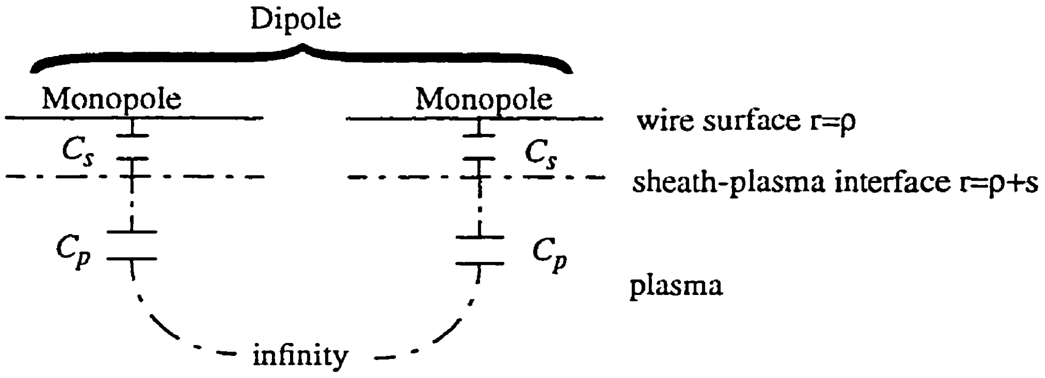

Figure 2-4. Dipole capacitance as a sum of plasma and sheath contributions from two monopoles.

$$C_s = 2\pi\varepsilon_0\left[\ln\left(\frac{\rho+s}{\rho}\right)\right]^{-1} \tag{2-6}$$

To account for the collisional losses of the sheath, the permittivity of the vacuum layer needs to be modified by introducing a sheath conductivity σ_s which will be derived in Section 2.6.2, and eq. (2-6) can be rewritten as

$$C_s = 2\pi\left(\varepsilon_0 - \frac{j\sigma_s}{\omega}\right)\left[\ln\left(\frac{\rho+s}{\rho}\right)\right]^{-1} \tag{2-7}$$

Consequently, the resulting distributed capacitance for the two-conductor cylindrical capacitor is the series sum of the respective monopole capacitances as depicted in Fig. 2-4,

$$C = \frac{C_p C_s}{(C_p + C_s)} = \frac{2\pi\varepsilon_0\sqrt{K'K}\left(1 - \frac{j\sigma_s}{\omega\varepsilon_0}\right)}{\ln\left(\frac{\rho+s}{\rho}\right)\sqrt{K'K} + \ln\left(\frac{l}{\rho+s}\right)\left(1 - \frac{j\sigma_s}{\omega\varepsilon_0}\right)} \tag{2-8}$$

This is the capacitance per unit length for a monopole. Adachi [7] defined a dipole capacitance per unit length as half the above, a procedure which is unnecessary here.

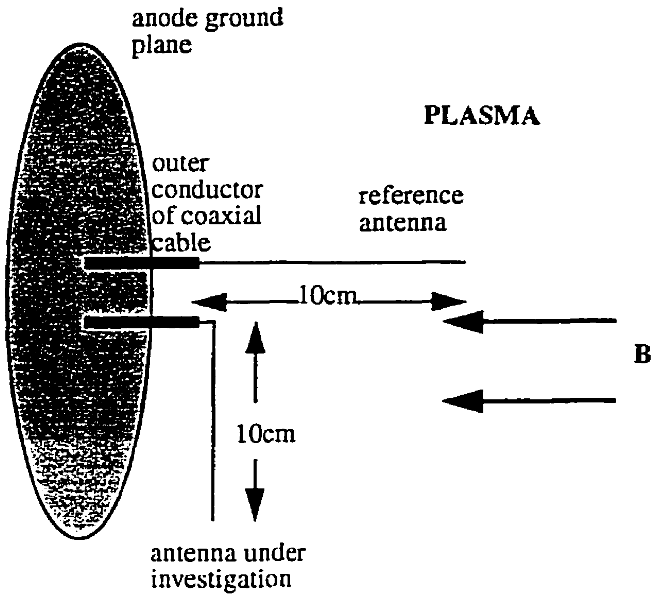

Figure 2-5. Laboratory arrangement of monopoles.

2.5 Input Impedance of Antenna

Having established the expressions for distributed inductance and capacitance, the input impedance of the dipole antenna may be derived by simple substitution of these parameters into the general transmission-line equations. Because of the existence of the extra coaxial section to which the antenna is attached as indicated in Fig. 2-5, its respective impedance contribution must also be included in the calculations. Considering the experimental reference plane location, one may use the position of the source in the transmission-line representation to divide the coaxial-monopole assembly into two distinct sections. The antenna may be represented by an open-circuited transmission-line segment for which a corresponding open-circuited input impedance is computed. Under the assumption of perfect conductors, the characteristic impedance of the transmission-line representation is given by

$$Z_{0oc} = \sqrt{\frac{R + j\omega L_{oc}}{G + j\omega C_{oc}}} = \sqrt{\frac{L_{oc}}{C_{oc}}} \tag{2-9}$$

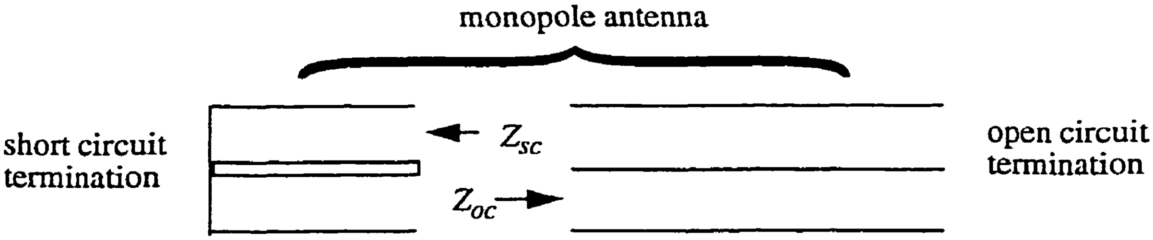

Figure 2-6. Total impedance $Z = Z_{sc} + Z_{oc}$ of the transmission line representing a a monopole antenna, as a sum of open-circuited and short-circuited sections.

where the dielectric conductance G has been absorbed into the distributed capacitance C utilizing the effective sheath conductivity. L and C were defined previously in eqs. (2-1) and (2-8). Subscript 'oc' indicates that parameters are evaluated using dimensions of the open-circuited section. The propagation constant γ is defined as

$$\gamma_{oc} = \sqrt{(R + j\omega L_{oc})(G + j\omega C_{oc})} \tag{2-10}$$

The input impedance of the dipole antenna is computed as

$$Z_{oc} = \frac{Z_{0oc}}{\tanh(\gamma_{oc} l_{oc})} \tag{2-11}$$

On the other hand, the coaxial section, being connected to the ground plane via an RF capacitor bypass, embodies a short-circuited segment of transmission line for which the input impedance may be readily calculated. Expressions similar to those of eq. (2-10) and (2-11) may be written and they lead to

$$Z_{sc} = Z_{0sc} \tanh(\gamma_{sc} l_{sc}) \tag{2-12}$$

The resultant impedance of the whole structure is simply the algebraic sum of the impedances of the two sections, i.e. the respective open-circuited and short-circuited impedance values

$$Z = Z_{oc} + Z_{sc} \tag{2-13}$$

2.6 Sheath and Plasma Parameters

2.6.1 Collision frequency

Electron-neutral collision frequency is calculated for the helium gas using the formula taken from Brown [10],

$$\nu = 5.93 \times 10^7 p_0 P_c \sqrt{u} \tag{2-14}$$

where u is the electron energy in eV, $p_0 = \frac{273p}{T_n}$, p is the pressure in Torr, T_n is the gas temperature, and P_c is the probability of collision.

2.6.2 Conduction losses in the sheath

In Section 2.4 the sheath gap was regarded as a lossless dielectric material which had not been specified. Although the electron population is sparse, there is a finite conductivity associated with electron-neutral collisions and electron absorption at the antenna surface. These losses may be taken into account by defining an equivalent sheath conductivity σ such that the sheath permittivity can be modified to reflect the non-ideal behaviour.

Following the analysis of Morin [9], the admittance for a cylindrical probe of radius ρ and length L with sheath thickness s is given by

$$Y = j\omega C = \frac{j\omega\pi\varepsilon_s L}{\ln\left(\frac{\rho + s}{\rho}\right)} \tag{2-15}$$

where $\varepsilon_s = \varepsilon_0 K_{0s}$, $K_{0s} = 1 - \frac{\omega_{ps}^2}{U\omega^2}$, $U = 1 - \frac{j\nu_s}{\omega}$, ω_{ps} is the angular plasma frequency in the sheath, and ν_s is the sheath collision frequency. Taking the real part of eq. (2-15) for $\omega \to 0$ and equating this to the DC conductance obtained from the characteristic of the Langmuir probe, one gets

$$G = n_s e^2 A \sqrt{\frac{2}{m\pi k T_e}} \tag{2-16}$$

where A is the surface area of the probe, one may define the sheath collision frequency as

$$\nu_s = \frac{1}{\rho \log\left(\frac{\rho + s}{\rho}\right)} \sqrt{\frac{\pi k T_e}{2m}} \tag{2-17}$$

It should be noted that the introduction of a sheath plasma density has complicated the vacuum sheath model since the sheath now resonates at its own plasma frequency. Fortunately, it was realized by Morin [9] that this plasma frequency is significantly smaller than the sheath collision frequency, so plasma resonance effects have been masked by the losses.

To represent the collision losses by a finite sheath conductivity, the sheath relative permittivity must be redefined as

$$K_{0s} = 1 - \frac{j\sigma_s}{\omega\varepsilon_0} \tag{2-18}$$

Comparing with the expression for sheath permittivity,

$$K_{0s} = 1 - \frac{\omega_{ps}^2}{\omega^2 + \nu_s^2} - \frac{j\omega_{ps}^2 \nu_s}{\omega(\omega^2 + \nu_s^2)} \tag{2-19}$$

one may deduce the conductivity to be

$$\sigma_s = \frac{n_s e^2}{m\nu_s} \tag{2-20}$$

The above evaluation for effective sheath conductivity is valid for an isotropic plasma. In the presence of a static magnetic field, particle transport in the direction perpendicular to the field lines is impeded as charged particles gyrate about the magnetic lines of force. This is believed to cause a reduction in particle flux to the antenna, consequently affecting the DC conductance of the probe. Such an effect is especially pronounced for an antenna aligned with the ambient magnetic field, and also in situations in which the sheath thickness is larger than the Larmor radius of the electron. Thus an additional complication of plasma magnetization is a decrease in the sheath thickness.

A formal treatment to properly address this issue would entail an assessment of the extent to which cross-field diffusion is hindered. A precise analysis which appropriately reflects the impedance variation with field strength is deemed too difficult and beyond the scope of this work. Determination of the degree to which sheath thickness is reduced is likewise impossible. As a consequence, effects of magnetization on the sheath will not be taken into account in the computation of the antenna conductance.

2.6.3 Sheath thickness

Determination of the sheath thickness requires knowledge of the probe potential with respect to the plasma. The following discussion lays the framework within which the floating potential of the probe may be determined theoretically [11].

For an electrically floating surface, plasma flow to the probe surface assumes the form of ambipolar diffusion. Electron flux (per unit area) to a cylindrical probe can be calculated for a Maxwellian distribution by integration utilizing distribution functions with the result being

$$\Gamma^{e}_{surface} = \frac{1}{4} n_{esurface} c_e = \frac{1}{4} n_0 e^{\frac{e\varphi_{surface}}{KT_e}} c_e \qquad (2\text{-}21)$$

where n_0 is the ambient plasma density and $c_e = \sqrt{\frac{8KT_e}{\pi m_e}}$ is the electron thermal velocity.

By continuity, the ion flux (per unit area) to the probe surface is equal in magnitude to the flux at the plasma-sheath boundary, thus

$$\Gamma^{i}_{surface} = \Gamma^{i}_{sheathedge} = \frac{1}{2}n_0 c_s \tag{2-22}$$

where $c_s = \sqrt{\frac{K(T_e + T_i)}{m_e + m_i}}$ is the ion acoustic speed. Equating eqs. (2-21) and (2-22), it follows that

$$\varphi_p = \frac{KT_e}{e}\left\{\frac{1}{2}\log\left(\left[\left(\frac{\pi m_e}{2m_i}\right)\left(1 + \frac{T_i}{T_e}\right)\right]\right)\right\} \tag{2-23}$$

The thickness of the sheath has been calculated using the empirical result of Kiel [12]. Two-dimensional effects arising from cylindrical geometry have not been included in the continuity relation, in the expectation that a planar estimate for the floating potential should suffice for the purpose of estimating the sheath thickness. The sheath thickness can be expressed as a function of the probe potential, and it is further related to various plasma parameters through the following relations, in which r_s and r_p are the sheath and probe radii:

$$R_s = \frac{r_s}{r_p} = 1 + \gamma^{-0.375}\tau(\alpha)\sqrt{\eta_{p\alpha}} \tag{2-24}$$

where

$$\eta_{p\alpha} = 1.16 \times 10^{4}\left(\frac{1+Z}{T_e + T_i}\right)|\varphi_p| \tag{2-25}$$

$$\gamma = \left(\frac{1}{1 + \frac{\alpha}{Q}}\right)\left(\frac{r_p}{\lambda_D}\right)^2 \tag{2-26}$$

$$\tau = 1.54(1 - 0.2\alpha^{0.35}) \tag{2-27}$$

and where Z is the ion charge, T_i is the ion temperature in degrees Kelvin, φ_p is the probe potential in volts, Q is the charge ratio of ions to electrons, and α is the ratio of ion to electron temperature. All subsequent calculations are based on parameters summarized in Table 2-1.

2.7 Summary of Parameters

Table 2-1 Numerical Values for Parameters Used in Theoretical Computations

parameter	value
θ_{oc}: angle between extended inner conductor and B	0 or $\frac{\pi}{2}$
θ_{sc}: angle between coaxial section and B	0
l: physical length of extended inner conductor	0.1 m
l_{oc}: inner conductor length taking into account "end effect"	0.106 m
l_{sc}: length of coaxial section	0.03 m
ρ_{oc}: inner conductor radius	0.00026 m
ρ_{sc}: radius of coaxial outer conductor	0.0011 m
f_p: plasma frequency	411 MHz to 990MHz
f_c: cyclotron frequency	0 to 1260 MHz
f_{uh}: upper hybrid frequency	411 MHz to 1602 MHz
electron temperature	0.2 eV
α: ion to electron temperature ratio	0.13
ν : collision frequency	23.3 MHz or 500 MHz
inner conductor bias relative to anode	-0.25 V to -2.2 V
s_{sc}: sheath thickness along coaxial section	0 m
s_{oc}: sheath thickness along inner conductor	0 to 13 Debye lengths

Chapter 3

EXPERIMENTAL PRELIMINARIES

3.1 General Overview of Experiment

The laboratory arrangement consists of a coaxial cable-monopole antenna assembly immersed in a helium discharge plasma as shown in Fig. 3-1. Experiments were conducted utilizing a 16-litre glass chamber in which an anode-monopole assembly of Fig. 2-5 was placed. Helium gas was let into the chamber to initiate a discharge by applying high DC voltage between the two electrodes. The gas pressure was maintained at approximately 50 mTorr over the duration of the measurements.

The coaxial cables are fed through a brass anode which approximates an infinite conducting plane. Field coils generate an axial DC magnetic field of variable strength controlled by the coil current. The axis of the monopole antenna of interest is oriented perpendicular to the magnetic field while the reference monopole is aligned with the magnetic field in order to provide density measurements by the detection of quarter-wave or higher-order resonances (Morin [9]).

The reflection coefficient from the plasma-immersed monopole was measured at the base of the antenna over a frequency range from 300 kHz to a few gigahertz using an HP 8753 C network analyzer. Antenna impedance as a function of frequency was deduced from the reflection coefficient measurement using simple transmission-line relations. Points of resonance were identified as the peaks of the conductance vs. frequency plot.

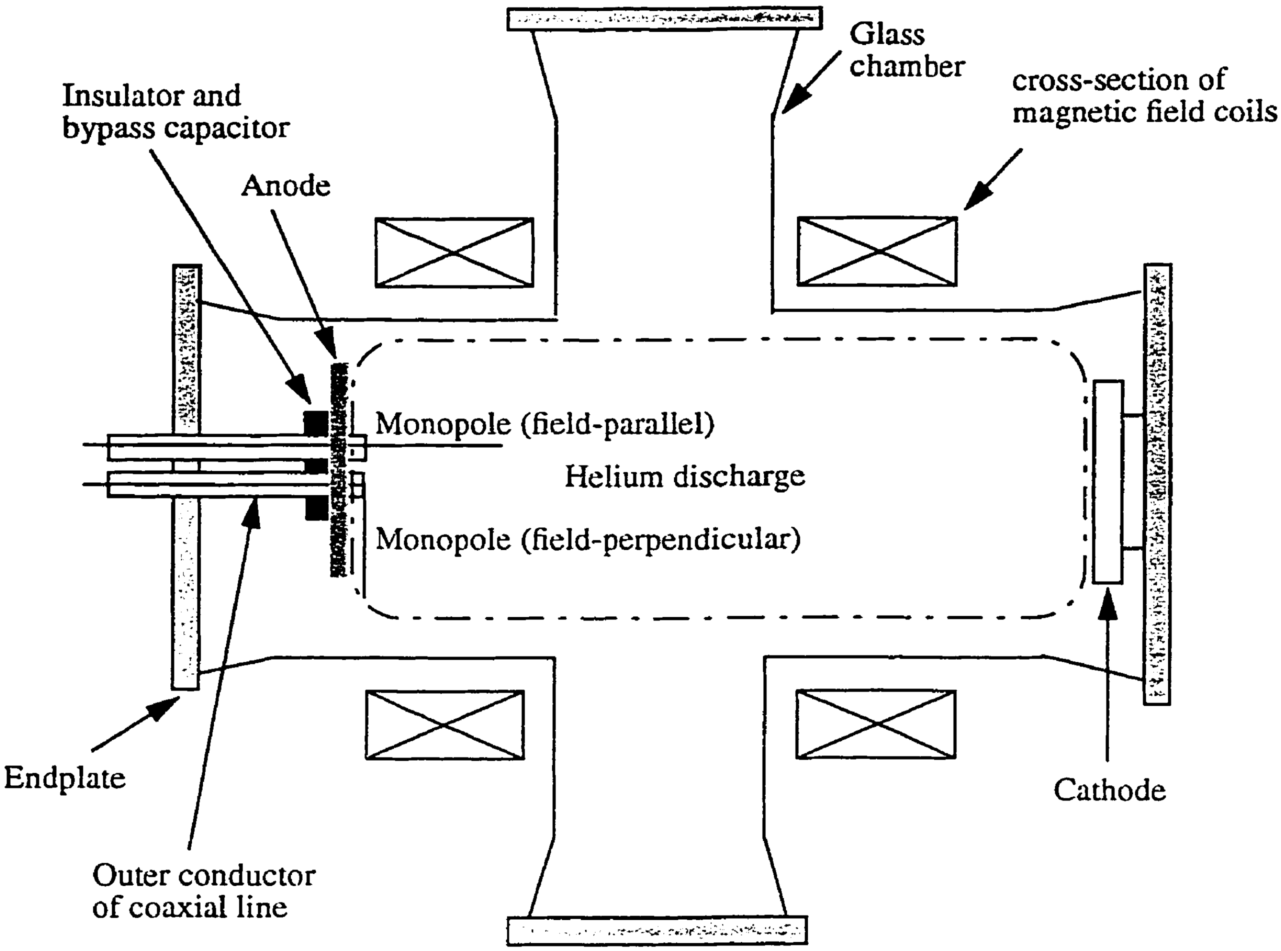

Figure 3-1. Plasma chamber and antenna-anode assembly.

3.2 Experimental Apparatus

3.2.1 Length of plasma-immersed coaxial cable

Observation of resonance phenomena along the antennas requires the least amount of interference from electromagnetic waves excited in sheaths over the surface of any structures other than the antenna of interest. In order to collapse the sheath around the coaxial cables, a bias voltage can be applied to the outer conductor relative to the anode. The requirement that the anode surface area be considerably larger than the total biased conductor surface area is a consequence of the need to maintain a constant anode potential with respect to the plasma. By ensuring a minimum ratio of 100 for a helium discharge, the anode potential remains relatively constant in spite of large variations in outer conductor bias. This sets an upper limit on the length of the coaxial cables immersed in the plasma for a given cable diameter. Ideally, the antennas should be mounted as far from the anode as possible in order to minimize wave interference due to reflections from the anode sheath. An examination of anode sheath waves by Baker [3] revealed that the effect of sheath wave penetration into the plasma may be significant at low frequencies. A length of 0.03 m for the coaxial cable extension was selected along with a cable outer radius of 0.0011 m.

3.2.2 Dimensions of monopole antennas

Baker's work [3] had shown a non-uniform magnetic field strength over the cross-section of the plasma chamber, especially toward the edge of the plasma. Therefore the antennas should be confined within the region of more uniform magnetic field toward the centre. This also serves to suppress plasma edge effects which may prevent laboratory conditions from approximating the unbounded plasma environment in which the OEDIPUS-C experiment was conducted. On the other hand, the antennas must be sufficiently long to provide a reasonable number of resonance frequencies for ease and precision of data analysis. It was decided that the reference antenna should have the same length as the field-perpendicular antenna of interest for comparison purposes. The wire radius has been chosen to be 0.00026 m and the wire length is 0.1 m.

3.2.3 DC bias of coaxial cable and antennas relative to anode

Sheath collapse along the coaxial cable was achieved by connecting the outer conductor to ground and applying a negative bias on the anode ground plane as depicted in Fig. 3-2. An anode bias setting of -0.75V to -0.8V relative to ground was maintained throughout the duration of measurements taken. On the other hand, the antenna under investigation was negatively biased with respect to the anode in order to expand the sheath region available for propagation. This was implemented by connecting the inner conductor of the coaxial line through the DC bias port of the network analyzer to a power supply as illustrated in Fig. 3-2. Different bias voltages were used to obtain different sheath thicknesses. A positive antenna bias was sometimes necessary in order to observe the effect of sheath collapse on wave propagation characteristics. Antenna bias ranged from -2.2V to +2.7V relative to the anode potential. It should be mentioned that surface waves do not necessarily depend on the ion sheath as a medium for propagation as Laurin's work [2] suggested, but sheath collapse does provide an increase in attenuation of unwanted waves that propagate along the outer conductor.

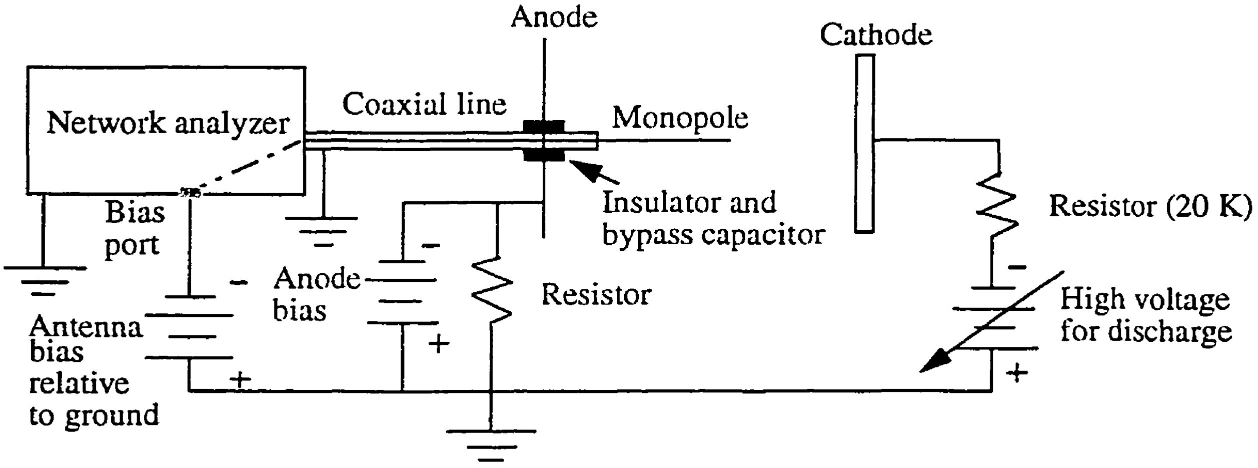

Figure 3-2. Antenna bias and discharge circuit.

3.2.4 RF capacitor bypass

It was noticed initially that the sheath resonance region of the impedance plots was dominated by background noises in the range below 500 MHz, rendering the observation of sheath wave effects very difficult. Therefore RF bypass capacitors were installed connecting the outer conductor of the coaxial cable to the anode ground plane. This provides an alternative current path at frequencies at which noise interference from the outside environment is believed to dominate the impedance, thus effectively eliminating the low frequency interference. Subsequent measurements showed dramatic improvement in reduction of noise.

3.2.5 Magnetic field measurement

Correlation between the coil current and the magnetic field strength was established by measuring the field strength using a Gaussmeter while varying the field current over the range of experimental conditions to be encountered. The use of a magnetic field probe enabled measurements to be taken for transverse and longitudinal orientations at locations inside the chamber which correspond to the positions of the monopoles. These measurements indicate that the field strength is fairly uniform throughout the region over which the antennas span with less than 5% difference over the dimensions of the antennas. The cyclotron frequency is related to the coil current by the empirically obtained approximate expression: $f_c(MHz) = 35I(A)$.

3.2.6 Antenna construction and calibration

Assembly of the antenna-anode system was performed as described in the following. A section of coaxial cable was taken and stripped of the dielectric and the outer conductor over a length of 10 cm, leaving only the inner conductor at the end of a coaxial line. This section of exposed inner conductor serves as the monopole. The exact lengths of the coaxial sections were determined by the Time Domain Reflectometry (TDR) technique which detects reflection from the open end of the coaxial cable and translates the time delay into a length factor. The monopole-coax was then positioned through the anode ground plane. An insulation ring was placed at the joint between the coaxial line and the anode, making possible the indepedent bias of the outer conductor from the anode. Connection of the anode ground plane to the outer conductor was established via RF bypass capacitors. The antennas were excited using an RF feedthrough, as can be seen in Fig. 2-5.

Calibration before impedance measurements was necessary in order to correct for the phase delay due to the section of coaxial line. This procedure enabled the placement of the reference plane to be at the base of the antennas, thus allowing meaningful measurement of the reflection coefficient. Calibration reference standards had to be manually constructed to take into account the existence of the coax. This was performed by preparing segments of coaxial line having the same length as the coaxial sections to which the antennas were attached. At the open end of the coaxial line, these reference segments were made short-circuited, open-circuited, and matched with a 50-ohm resistor. The short circuit was constructed by connecting the inner and outer conductors with copper foil, and the matched load was achieved by soldering two 100-ohm chip resistors in parallel between the inner and outer conductors.

3.3 Plasma Diagnostic Techniques

It should be emphasized that no specific instruments were introduced into the plasma chamber for the purpose of plasma diagnostics. Estimate of the electron temperature is based on the experimental results of previous work and has been assumed to be 0.2 eV throughout the calculations. The only instrumentation employed in the present work for diagnostic purposes is the antenna itself as a means of determining the plasma frequency. Morin [9] suggested three different techniques for estimating plasma frequency: the use of a Langmuir probe, detection of the quarter-wave resonance, and the antiresonance method. It was pointed out in his work that accuracy of the Langmuir probe measurement of plasma frequency relies on having a contamination-free environment which cannot be assured over a timespan of weeks or months. On the other hand, plasma frequency values obtained from detection of the quarter-wave resonance and the antiresonance method agree to within 20% of each other. However, Morin [9] pointed out that some ambiguity was inherent in a graphical estimate of the plasma frequency using the antiresonance method. As a result, the quarter-wave resonance method was chosen for density diagnostics of the plasma.

Morin [9] has outlined the method of quarter-wave resonance for antennas immersed in an isotropic plasma. A dipole antenna resonates first at the quarter-wave frequency at which the half-length of the antenna is equal to the quarter-wavelength of the propagating waves. The quarter-wave resonance frequency depends for the same antenna on the permittivity of the medium, i.e. in an isotropic plasma the resonance frequency moves to a higher value

$$f_r^2 = f_p^2 + f_{ro}^2 \tag{3-1}$$

where f_{r0} is the measured free space quarter-wave resonance frequency, and f_r is the quarter-wave resonance frequency measured for different plasma conditions. The plasma frequency can thus be derived from the shift of the resonance frequency. In the presence of a steady magnetic field, the equation used to calculate the plasma frequency is modified by replacing K_0 with K' to approximately take into account the effect of the medium anisotropy, which yields

$$f_p = \sqrt{(f_r^2 - f_c^2)\left[1 - \left(\frac{f_{ro}}{f_r}\right)^2\right]} \tag{3-2}$$

Derivation of eq. (3-2) can be found in the Appendix.

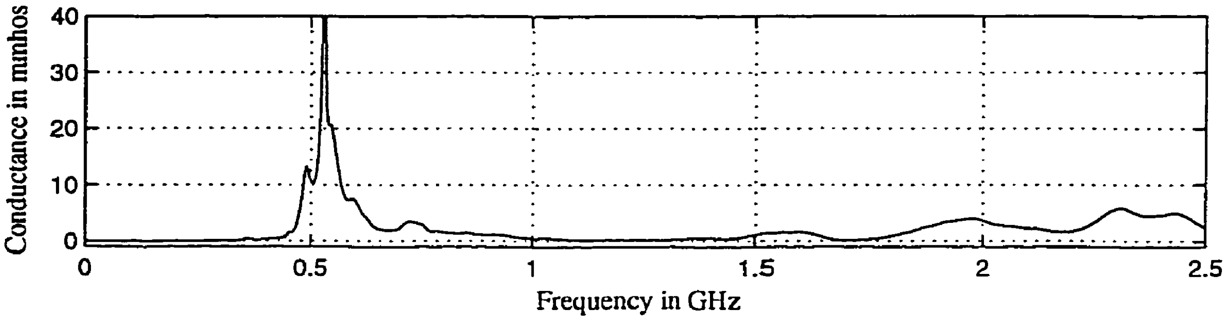

Figure 3-3. Measured free space quarter-wave resonance at 532 MHz for the field-parallel antenna.

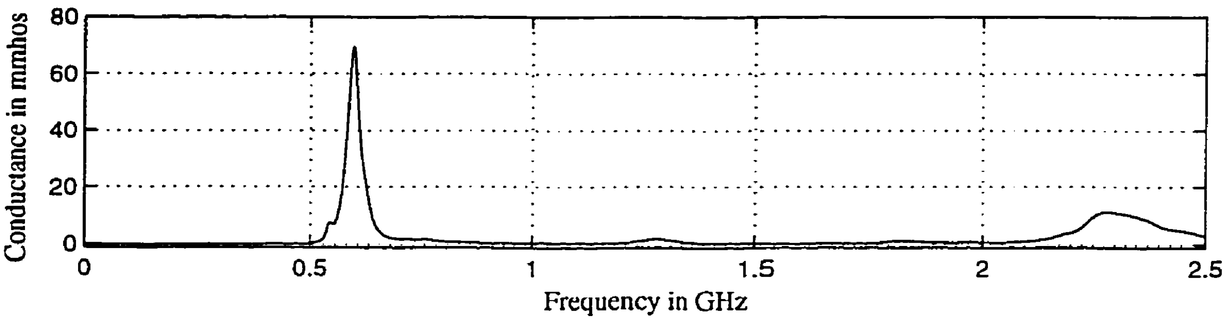

Figure 3-4. Measured free space quarter-wave resonance at 598 MHz for the field-perpendicular antenna.

Caution was taken when attempts were made to identify the quarter-wave resonance from the experimental admittance results. To properly identify the quarter-wave resonances, it is assumed that the quarter-wavelength in the free space medium is equal to the total length of the monopole-coaxial section. The peak located closest to the free space estimate in experimental conductance plots is then identified as the quarter-wave resonance. Figures 3-3 and 3-4 display free space conductance measurement of the parallel and perpendicular antennas, respectively. It has been realized that the effect of elongation of the coaxial section on the apparent antenna length cannot be ignored. Consequently, the monopole length involved in the free space estimate for the resonant frequency includes the length of the coaxial line section to which the antenna is attached. Furthermore, the end-effect on the monopole has also been included to take into account the apparent elongation factor of roughly 6% (Jordan and Balmain [13]). The discrepancy

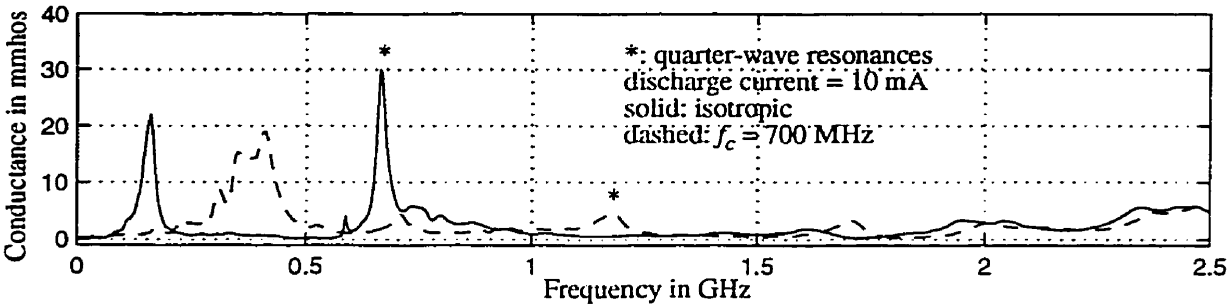

Figure 3-5. Measured quarter-wave resonance of field-parallel antenna in an isotropic plasma compared with the value when the ambient magnetic field is strong.

between this estimate and the presumed resonance in the experimental data is reasonable at about 5%. Some experimental measures were taken as explained in the following to further ensure the correct identification of these resonances. In spite of the fixed length of the antennas in the actual experiments performed, some variation of the length was implemented while the antenna-anode assembly was outside the plasma chamber. Different lengths of solder wire were attached to the end of the antennas and measurement of reflection coefficient was taken for each length. The longitudinal resonances were then identified for the free space case by noting the frequency shift corresponding to each variation relative to the default antenna length. This has established, beyond any doubt, that these are indeed the quarter-wave resonances sought. It also provides a reference for comparison when examining measurements taken in the anisotropic plasma medium. In addition, by comparing with free space measurements performed outside the glass chamber, it was observed that the effect of unwanted reflections from the chamber walls is relatively small.

Plasma frequencies deduced from experimental quarter-wave resonance maxima for the reference antenna are characterized by values consistently higher than results previously obtained at the centre of the chamber. Laurin [2] had pointed out that the density inhomogeneity accounts

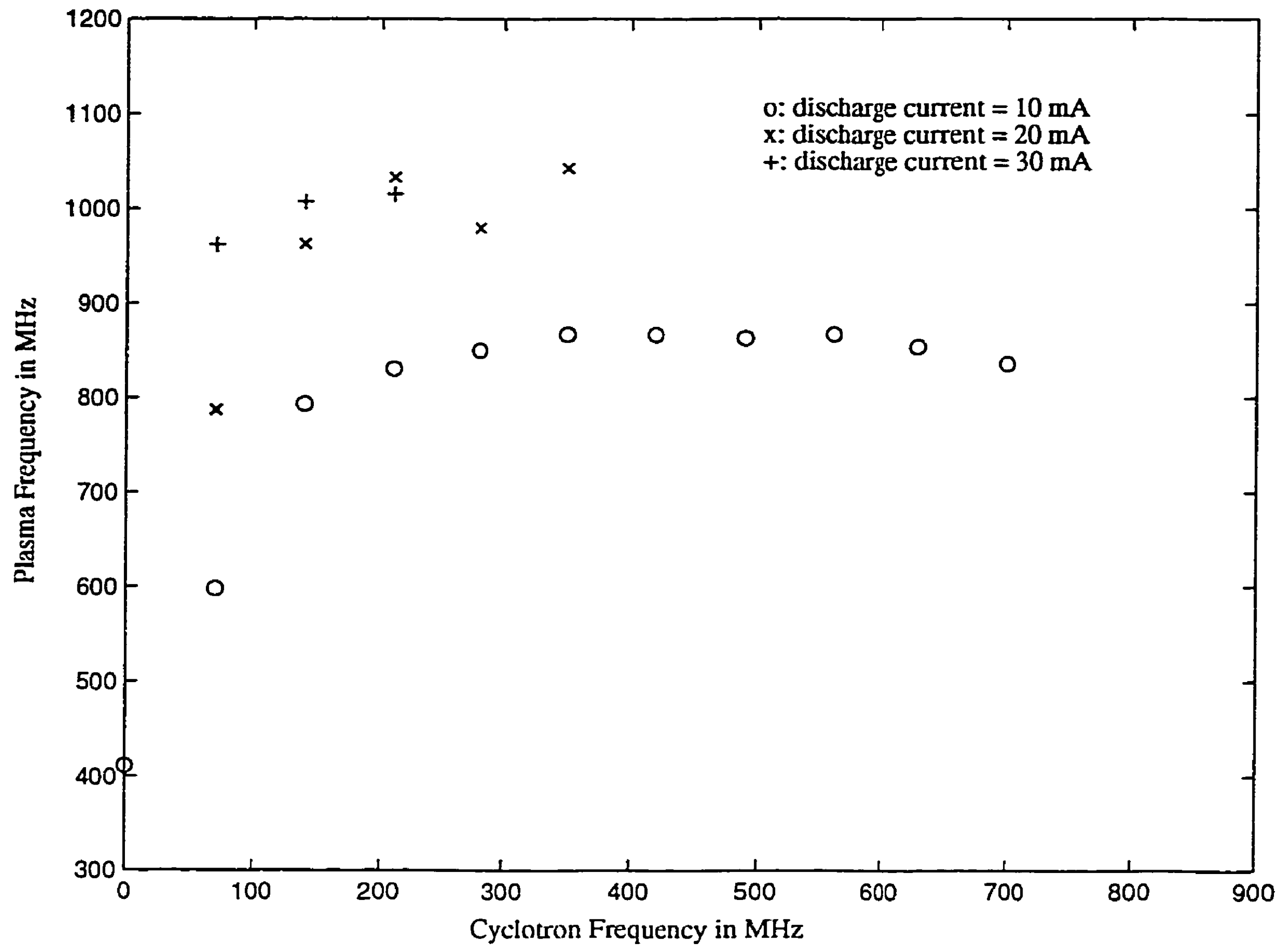

Figure 3-6. Plasma frequency derived from measured quarter-wave resonance of field-parallel antenna for various discharge currents.

for plasma frequency values up to 25% higher near the anode than that of the plasma core. For cyclotron frequencies above 280 MHz, these results also exhibit little variation in density with increasing magnetic field strength for various discharge currents. When the ambient magnetic field is allowed to increase, the dominant conductance peak gradually subsides in magnitude and eventually becomes absorbed by the background. The solid curve in Fig. 3-5 depicts the strength of the quarter-wave resonance in the absence of an ambient magnetic field compared with the same resonance in the presence of strong ambient magnetic field indicated by the dashed curve. For discharge currents above 20mA, the conductance features flatten out considerably with increasing cyclotron frequency, thus obscuring the quarter-wave resonance. This has rendered impossible the deduction of plasma frequency from experiments. As a result, the plasma frequency estimate obtained from the detection of quarter-wave resonance is incomplete for higher discharge currents. It is for this reason that the ensuing comparison between theory and experiment should be limited to situations in which plasma frequencies are below 870 MHz. Figure 3-6 displays the values of plasma frequency obtained from the shift of the quarter-wave resonance relative to the free space admittance maximum.

Alternatively, determination of the plasma frequency may be carried out by the antiresonance method in which the phase of the impedance undergoes zero crossing near the upper hybrid frequency for an anisotropic plasma. However, ambiguity arises when one attempts to locate the exact frequency of upper hybrid resonance because of the slow variation of phase with frequency near resonance. In fact, the phase remains relatively invariant over a wide range of the spectrum which renders the task very difficult. For low cyclotron frequencies, resistance plots could be utilized to identify the upper hybrid frequency. As the magnetic field strength is raised, however, the upper hybrid resistance peak became dispersed and could no longer be identified. Thus the detection of the quarter-wave resonance remains most appropriate for this purpose.

Chapter 4

EXPERIMENTAL ADMITTANCE VS. THEORETICAL CALCULATIONS

4.1 Introduction

The notion of passband and stopband characteristics for sheath wave propagation has been utilized previously by Laurin [2] and Baker [3]. Their work suggests the existence of sheath-wave passbands, certain frequency ranges characterized by relatively low attenuation levels. The criterion for classification of passbands and stopbands is based on the relative magnitude of the real and imaginary parts of the propagation constant. Frequency ranges in which the real part (attenuation) exceeds the imaginary part (wavenumber) are considered as stopbands, and passbands are defined as those ranges in which the imaginary part is greater than the real part. Propagation constants generated using transmission-line theory are further subclassified into stopbands and passbands of various degrees. These theoretical stopbands and passbands can be displayed on CMA diagrams, thus helping in the interpretation of the theory while presenting an overview of the propagation characteristics.

4.2 Field-Parallel Antenna

4.2.1 Theoretical propagation constants

The propagation constant for the open-circuited section of the transmission line (representing the extended inner conductor of the coaxial cable) was computed using eq. (2-12) for various plasma conditions. Figure 4-1 provides a comparison of its behaviour in the presence and absence of a finite sheath for a case in which $f_c < f_p$. In view of Fig. 4-1 (a) for the

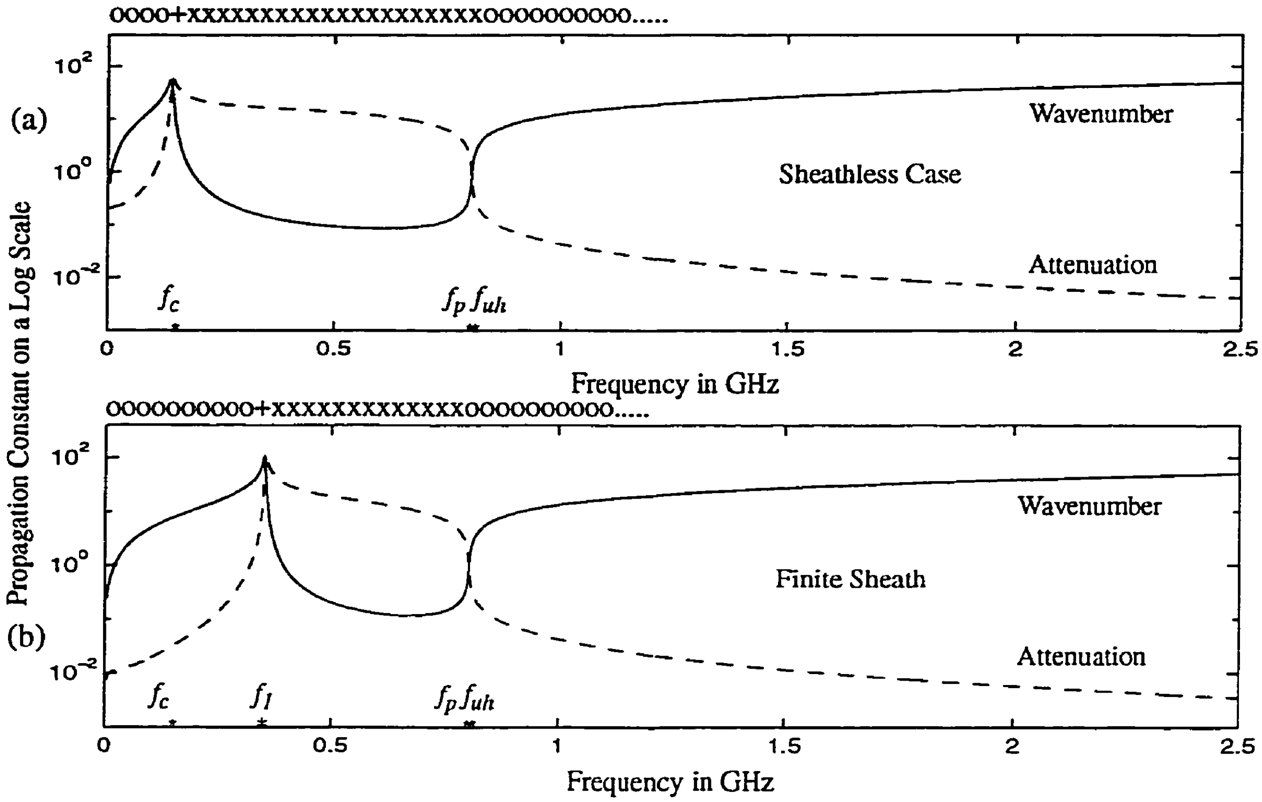

$\theta = 0$ degrees
$l_{oc} = 0.106$ m
$\rho_{oc} = 0.00026$ m
$\nu = 23.3$ MHz
$f_p = 793$ MHz
$f_c = 140$ MHz
$f_{uh} = 805$ MHz
a): $s = 0$ m

b): $s = 0.00046031$ m $= 12.2075\ \lambda_D$
$T_e = 0.2$ eV
$\sigma = 3.2127\text{e-}8$
o: propagation $\{\text{abs}[\text{real}(k_{oc})/\text{imag}(k_{oc})] > 1\}$
x: cutoff $\{\text{abs}[\text{real}(k_{oc})/\text{imag}(k_{oc})] < 1\}$
+: $\{1 < \text{abs}[\text{real}(k_{oc})/\text{imag}(k_{oc})] < 20\}$
solid: imag (k_{oc}) = wavenumber
dashed: real (k_{oc}) = attenuation
$f_l = 359$ MHz

Figure 4-1. Field-parallel antenna theory: real and imaginary parts of propagation constants for a case in which $f_c < f_p$.

sheathless case, the present work predicts a low frequency passband from zero to a cutoff frequency f_c. For the sheathed antenna of Fig. 4-1 (b), this cutoff frequency shifts upward from the cyclotron frequency to a frequency f_l . It should be mentioned that f_l is sheath-dependent and is not simply related to either the plasma frequency or the cyclotron frequency. It should be noted also that f_l is lower than the $\frac{f_{uh}}{\sqrt{2}}$ cutoff frequency predicted by Laurin [2] for the planar geometry.

Further, Laurin's full-wave solutions reveal the existence of two passbands: a low-

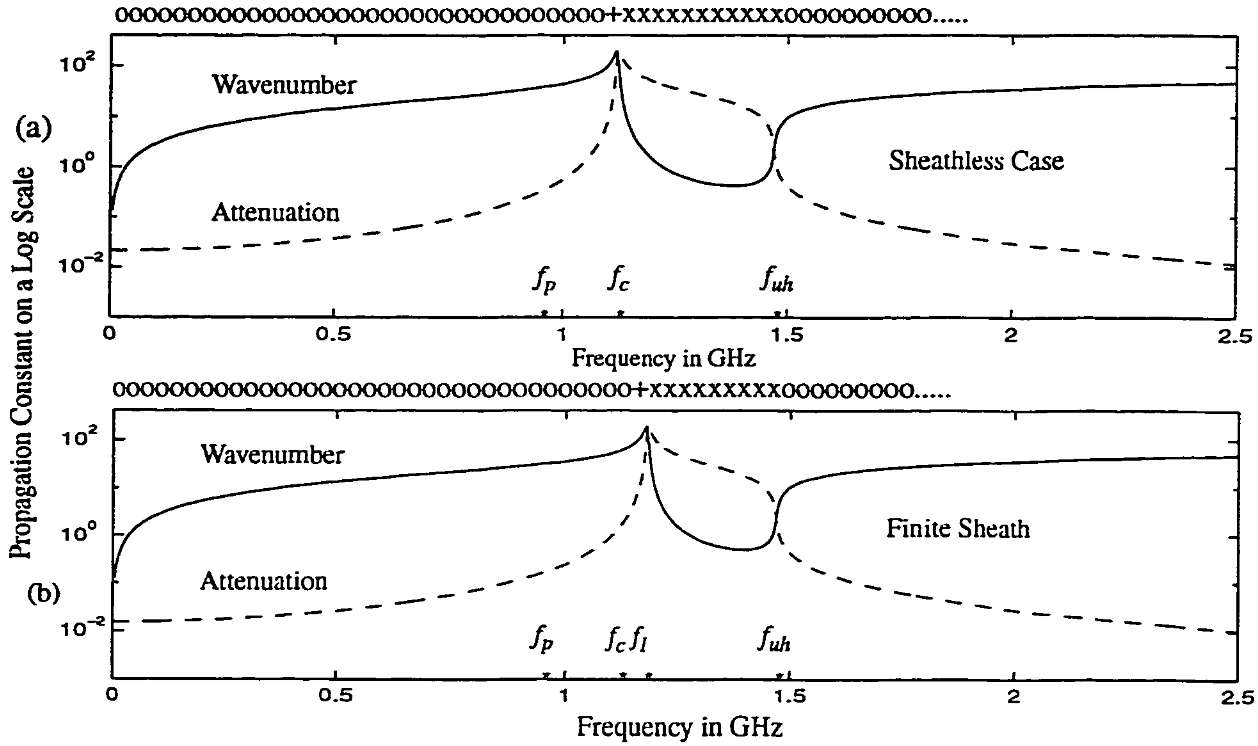

$\theta = 0$ degrees
$l_{oc} = 0.106$ m
$\rho_{oc} = 0.00026$m
$\nu = 23.3$ MHz
$f_p = 950$ MHz
$f_c = 1120$ MHz
$f_{uh} = 1469$ MHz
a): $s = 0$ m

b): $s = 0.00040199$ m $= 12.7714\ \lambda_D$
$T_e = 0.2$ eV
$\sigma = 4.2287\text{e-}8$
o: propagation {abs[real(k_{oc})/imag(k_{oc})] > 20 }
x: cutoff {abs[real(k_{oc})/imag(k_{oc})] < 1 }
+: { 1 < abs[real(k_{oc})/imag(k_{oc})] < 20 }
$f_l = 1177$ MHz
solid: imag (k_{oc}) = wavenumber
dashed: real (k_{oc}) = attenuation

Figure 4-2. Field-parallel antenna theory: real and imaginary parts of propagation constants for strong ambient magnetic field case in which $f_c < f_p$.

attenuation passband up to the cyclotron frequency and a relatively high-attenuation secondary passband from the cyclotron frequency up to $\frac{f_{uh}}{\sqrt{2}}$. This is quite different compared to the transmission-line calculations which predict a very-low-attenuation passband with no change in characteristics at the cyclotron frequency. Thus the approximate transmission-line theory for the cylindrical conductor displays a significant departure in propagation characteristics compared to the planar full-wave solutions. For situations in which the cyclotron frequency is greater than the plasma frequency, as in Fig. 4-2, the transmission-line model predicts a cutoff higher than $\frac{f_{uh}}{\sqrt{2}}$. It

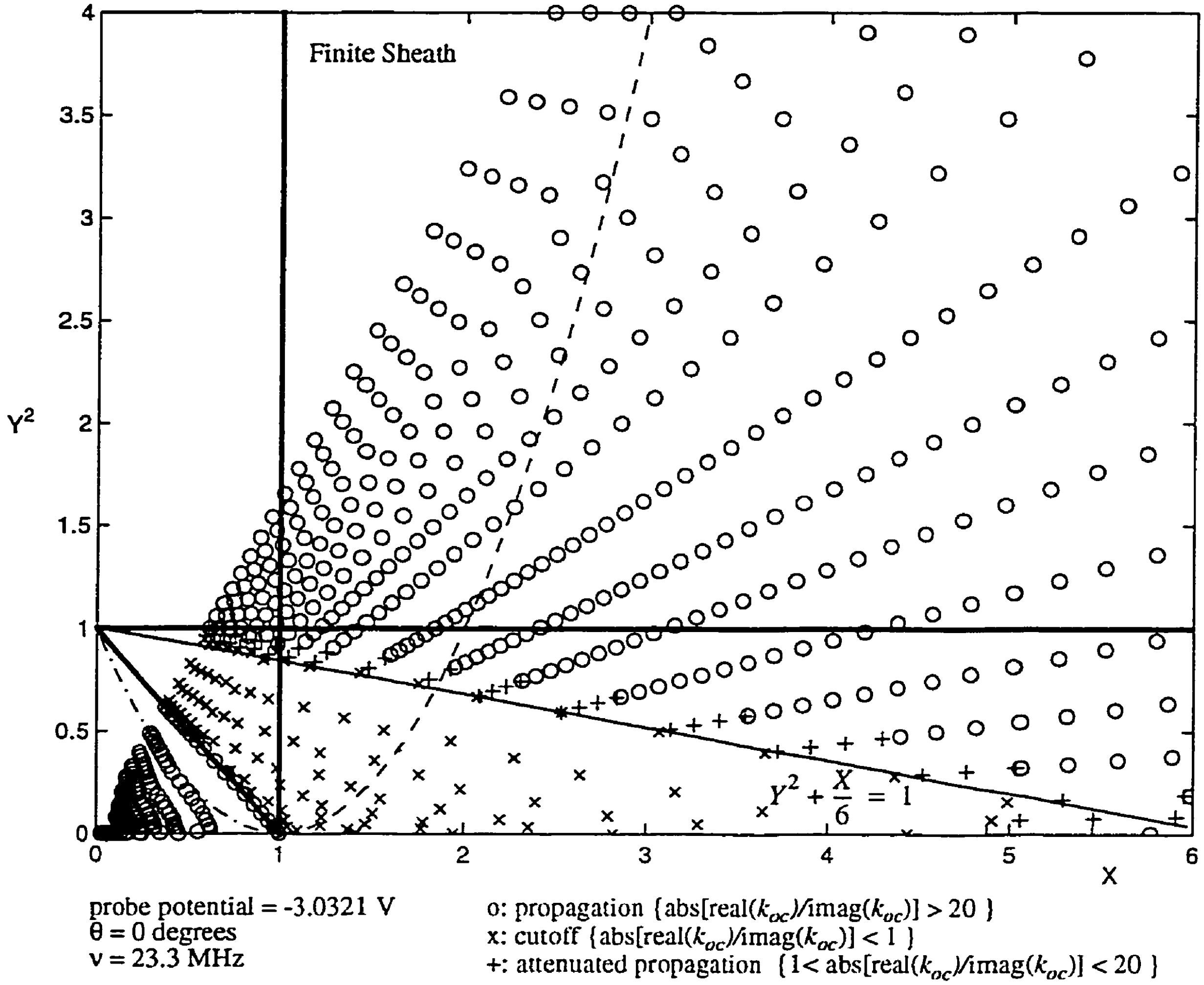

Figure 4-3. Field-parallel antenna theory: propagation characteristics displayed on a CMA diagram. Note the cutoff boundary approximated by $Y^2 + \frac{X}{6} = 1$.

should be noted that Fig. 4-2 displays the propagation constant for a case in which the normalized plasma parameters are comparable to those encountered in the OEDIPUS-C experiment. Like Fig. 4-1, Fig. 4-2 suggests the existence of a very-low-attenuation passband at low frequencies.

4.2.2 Display of propagation characteristics by CMA diagrams

CMA (Clemmow, Mullaly, Allis) diagrams may now be utilized to provide an overview of the theoretical propagation characteristics (Jordan and Balmain [13]). For the parallel

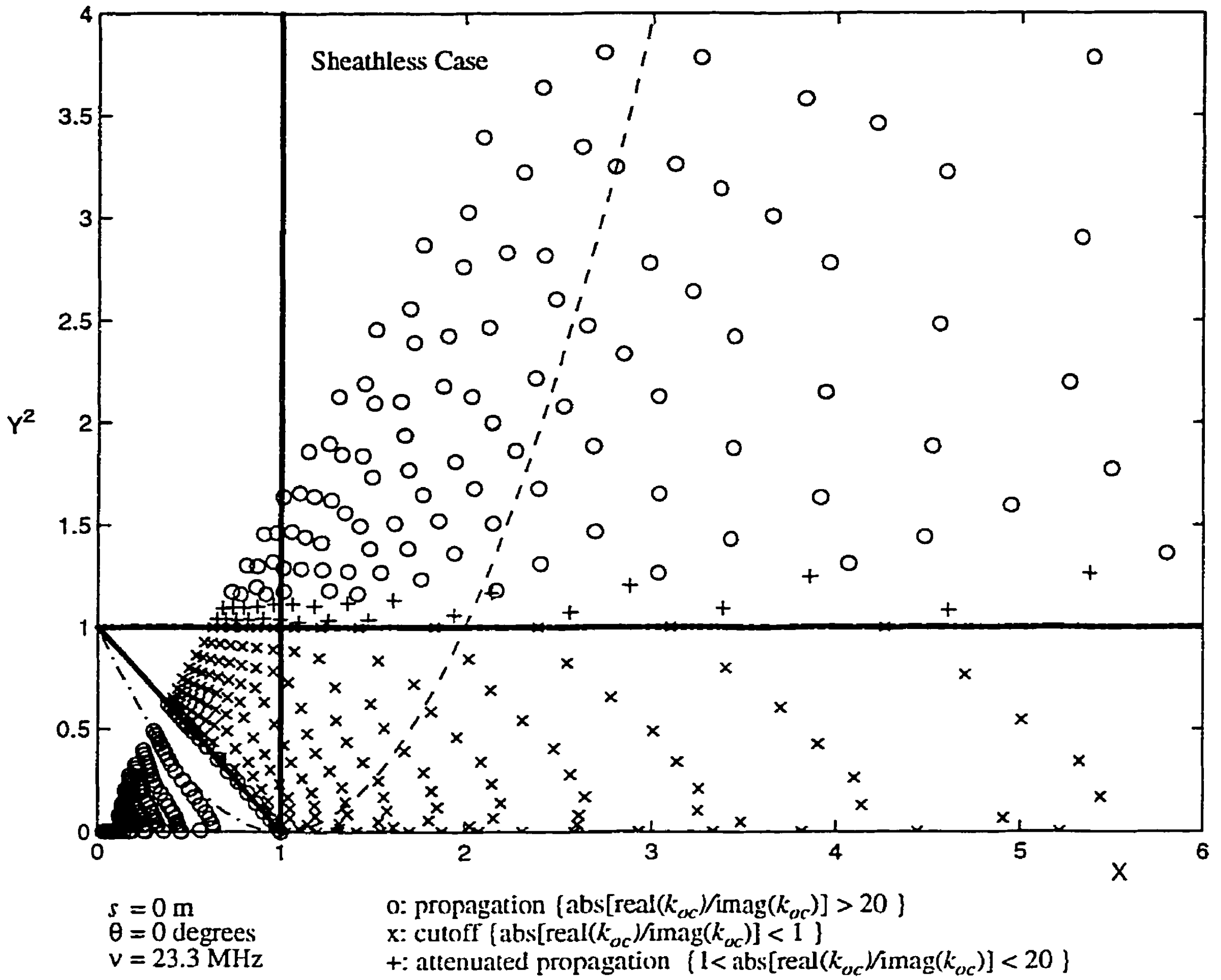

Figure 4-4. Field-parallel antenna theory: CMA diagram for the sheathless case.

orientation, Fig. 4-3 displays various passbands and stopbands for a wide range of plasma conditions. The lower 11 curves are calculated results based on actual experimental parameters encountered in the laboratory whereas the upper 8 curves are computed for cases of highly magnetized plasma, similar to the conditions encountered on OEDIPUS-C. Each ray of symbols corresponds to a specific ratio of plasma to cyclotron frequencies. Tracing inwards from the outermost point of each ray represents a sweep in source frequency from zero upwards. Regardless of the specific plasma conditions, a passband with virtually no attenuation is always present at low frequencies, as represented by the circles in the CMA diagram. This is followed by a transition into a stopband in which strong attenuation dominates as indicated by the x-marks. The transition occurs along a line given approximately by $Y^2 + \frac{X}{6} = 1$. Above the upper hybrid frequency, propagation resumes with little attenuation. For the sheathless antenna, Fig. 4-4 summarizes the propagation characteristics displaying a low-frequency passband below the cyclotron frequency. Behaviour of predicted passbands and stopbands above the plasma frequency for the sheathless antenna remains similar to the situation in which the sheath is present.

4.2.3 Observation of admittance features

Quarter-wave resonance: bias dependence and plasma density variation. As described in Section 3.3, this feature is characterized by a rapid decay in magnitude of the quarter-wave resonance with increasing cyclotron frequency for high discharge currents, thus severely limiting the extent to which plasma frequency can be determined. In addition, the quarter-wave resonance frequency has been observed to be dependent on conditions of applied bias as well as antenna orientation. More specifically, the quarter-wave resonance frequency for positive bias is consistently lower than that for negative bias regardless of the ambient magnetic field strength. This is believed to be a consequence of local plasma depletion due to the positive applied bias drawing excessive electron current to the probe, thus reducing the surrounding plasma density.

Sheath wave resonances: characterization by bias dependence. Experimental measurement of the antenna admittance reveals appreciable variation of low frequency characteristics with applied DC bias in the presence of a weak magnetic field. In particular, for the monopole parallel to the ambient magnetic field, the dominant low frequency conductance

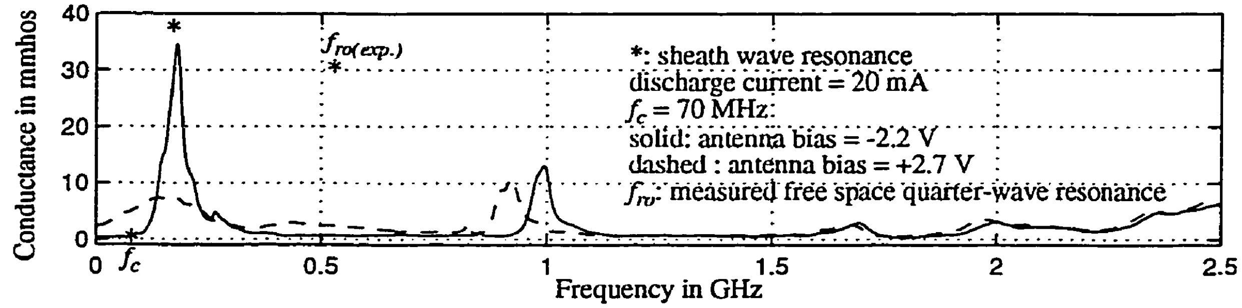

Figure 4-5. Field-parallel antenna experiments: influence of applied bias on low-frequency resonance, for very low ambient magnetic field.

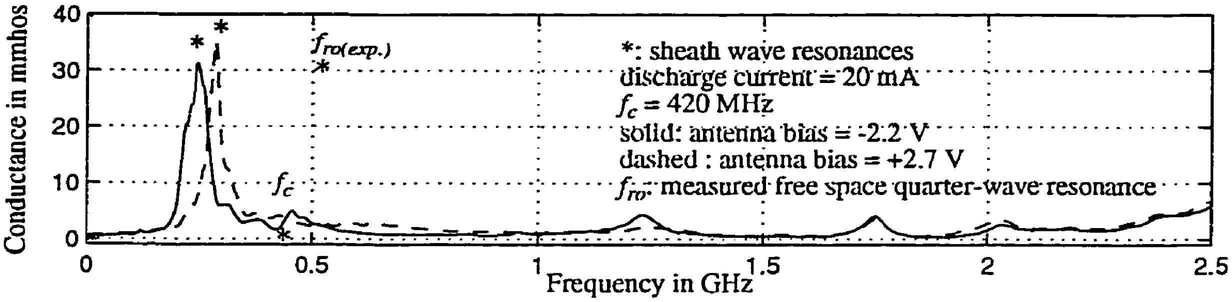

Figure 4-6. Field-parallel antenna experiments: bias effect at higher ambient magnetic field, compared with Fig. 4-5.

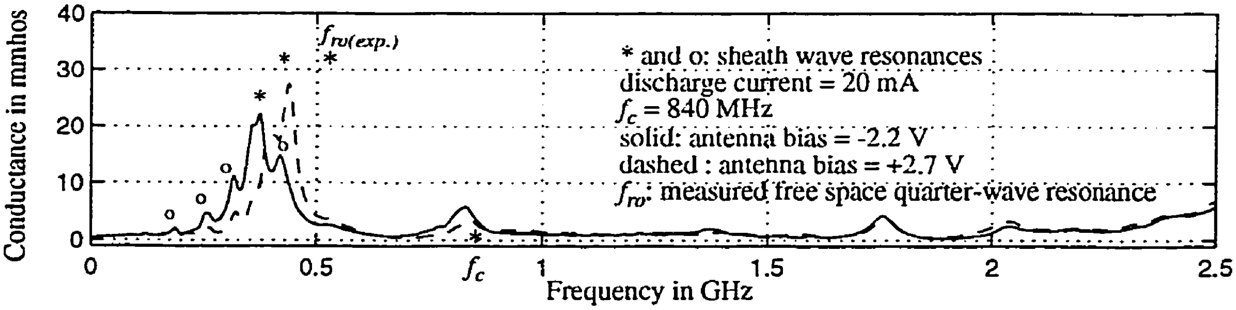

Figure 4-7. Field-parallel antenna: experiments: bias effects for a magnetic field twice that of Fig. 4-6.

peak near 200 MHz observable for negative antenna bias at low cyclotron frequencies is strongly suppressed by the application of a positive bias. Figure 4-5 shows this effect, indicating the extent to which the low frequency resonance is suppressed by positive bias. This evidence suggests that these resonances can be accounted for by propagation of sheath waves. It was observed that variation of the bias setting between -2.2V and -0.2V produced little change in admittance at low frequencies at which sheath resonances are observed, and likewise bias variation between different positive settings of +2.7V and +1.7V yields little observable effect.

The high magnitude and very narrow bandwidth of the dominant low-frequency conductance peak are indicative of its lying in some low-attenuation sheath wave passband. For higher cyclotron frequencies, however, the effect of bias on the magnitude of this particular conductance peak diminishes. This is obvious from Fig. 4-6 which compares similar-magnitude resonances of a positively and a negatively biased antenna. This observation can be interpreted using the work of Mushiake [14] which predicts propagation of surface waves along a conductor in the absence of a sheath. The introduction of a sheath produces a more highly-attenuated passband between the cyclotron frequency and $\frac{f_{uh}}{\sqrt{2}}$, in addition to the primary passband below the cyclotron resonance. Consequently, for a weak ambient magnetic field, sheath wave resonances are observable above the cyclotron frequency in the secondary passband only for negative biasing. As the cyclotron frequency increases above the characteristic frequencies of sheath wave resonances, propagation now occurs in the primary passband regardless of bias conditions and therefore no appreciable difference in resonance strength can be observed. The resonance frequency nevertheless continues to be strongly influenced by the applied DC bias.

A further observation is the development of resonance spikes (indicated by the circles in Fig. 4-7) clustered about the aforementioned conductance peak as the cyclotron frequency continues to increase. This phenomenon is also related to sheath wave resonances because of their apparent suppression in magnitude by the application of a positive antenna bias. These resonance spikes are confined within the passband predicted by Laurin [2] between DC and the cyclotron frequency and appear at regular intervals. Multiple resonances reported by Laurin [2] were not observed experimentally due to the narrowness of the secondary high-attenuation passband from the cyclotron frequency up to $\frac{f_{uh}}{\sqrt{2}}$.

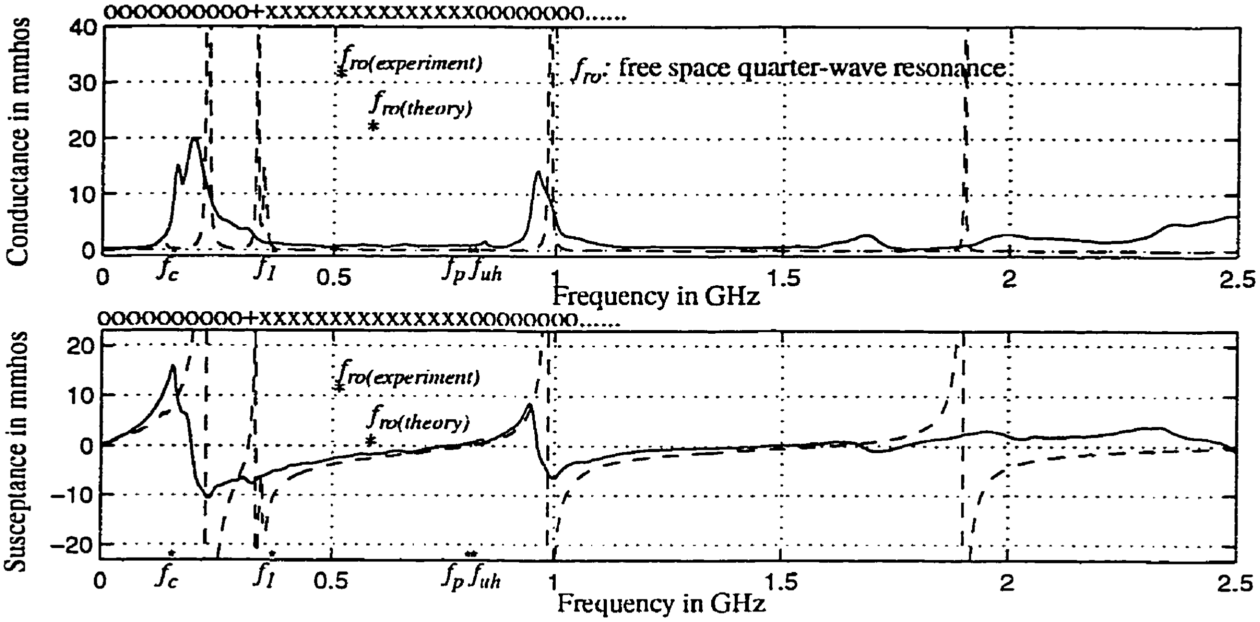

solid: experiment, dashed: theory

experimental conditions:

discharge current = 10 mA
$f_c = 140$ MHz
antenna bias relative to anode = -2.2 V

theoretical parameters:

$\theta = 0$ degrees
$l_{oc} = 0.106$ m, $l_{sc} = 0.03$ m
$\rho_{oc} = 0.00026$ m, $\rho_{sc} = 0.0011$ m
probe potential = -3.0321 V
$T_e = 0.2$ eV

$f_p = 793$ MHz
$f_c = 140$ MHz
$f_{uh} = 805$ MHz
$\nu = 23.3$ MHz
$s = 0.00046031$ m $= 12.2075\ \lambda_D$
$\sigma = 3.2127\text{e-}8$
o: propagation {abs[real(k_{oc})/imag(k_{oc})] > 20 }
x: cutoff {abs[real(k_{oc})/imag(k_{oc})] < 1 }
+: { 1 < abs[real(k_{oc})/imag(k_{oc})] < 20 }
$f_l = 359$ MHz

Figure 4-8. Field-parallel antenna: experimental admittance vs. theoretical results, for low magnetic field.

4.2.4 Comparison with transmission line computation

Utility of the transmission-line representation for plasma-immersed antennas suffers inherently from the premise of TEM mode propagation upon which all calculations are based. Its validity may now be assessed by comparing with experiments before extending its application to the field-perpendicular antenna. Computation of input admittance is implemented by the self-consistent transmission-line theory derived in Chapter 2. Plasma and antenna parameters are selected to simulate conditions encountered in the experiments. In particular, plasma frequency values extracted from experimental admittance data are directly substituted into the numerical

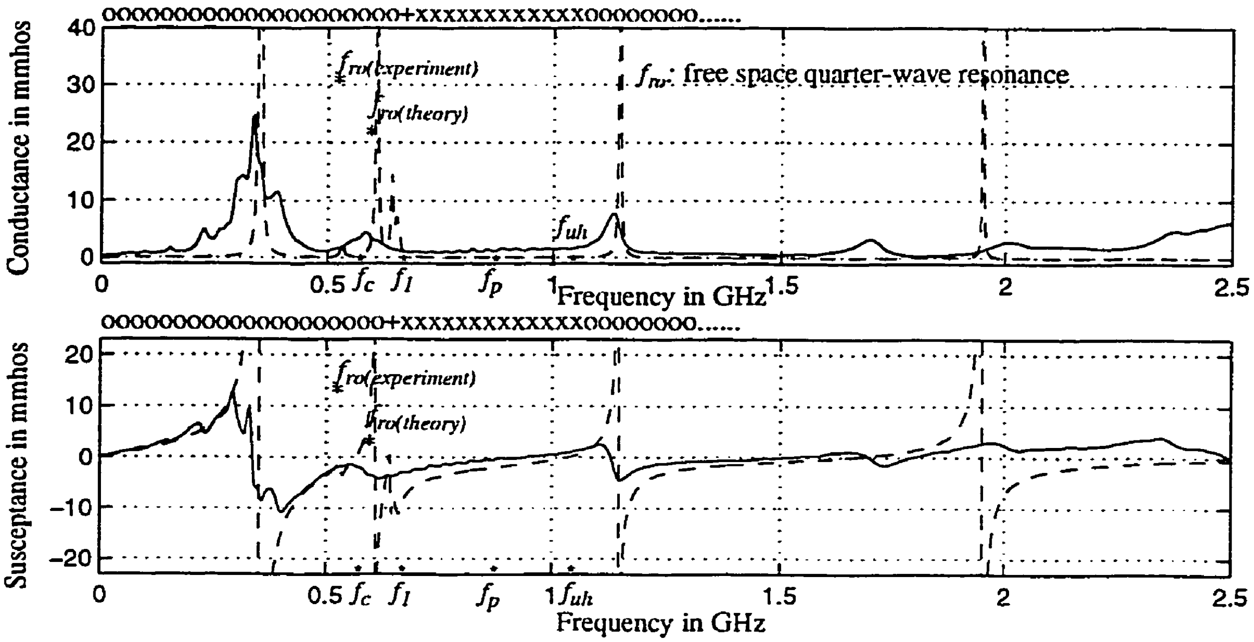

solid: experiment, dashed: theory

experimental conditions:

discharge current = 10 mA
f_c = 560 MHz
antenna bias relative to anode = -2.2 V

theoretical parameters:

θ = 0 degrees
l_{oc} = 0.106 m, l_{sc} = 0.03 m
ρ_{oc} = 0.00026 m, ρ_{sc} = 0.0011 m
probe potential = -3.0321 V
T_e = 0.2 eV

f_p = 867 MHz
f_c = 560 MHz
f_{uh} = 1032 MHz
ν = 23.3 MHz
s = 0.00043052 m = 12.4828 λ_D
σ = 3.6811e-8
o: propagation {abs[real(k_{oc})/imag(k_{oc})] > 20 }
x: cutoff {abs[real(k_{oc})/imag(k_{oc})] < 1 }
+: { 1 < abs[real(k_{oc})/imag(k_{oc})] < 20 }
f_l = 657 MHz

Figure 4-9. Field-parallel antenna: experiment/theory comparison for high magnetic field.

calculation procedure, the result of which is then superposed on the experimental admittance plot to reveal the extent to which theory accurately describes the propagation phenomenon.

Experimental vs. theoretical admittance: passbands and stopbands. Figure 4-8 depicts experimental admittance and its theoretical counterpart for a specific set of plasma conditions. In the frequency range of 1.5 GHz and above, there is strong disagreement between theory and experiment as expected. This high frequency region displays the limitations of the transmission-line theory which is only applicable to TEM waves and cannot predict either radiation or its

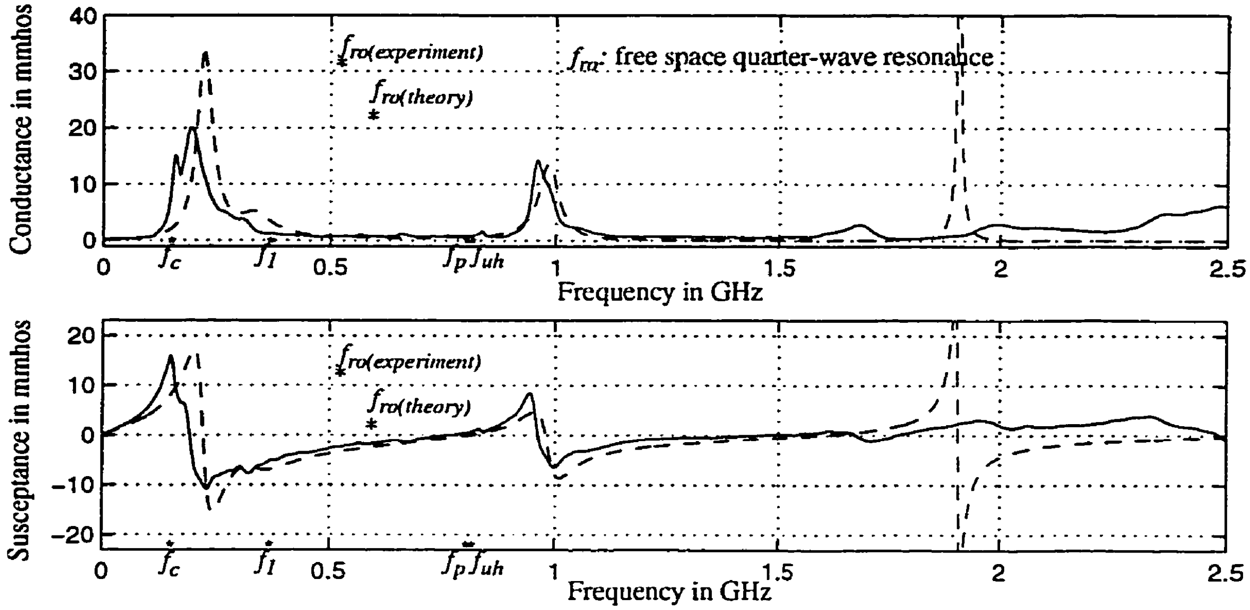

solid: experiment, dashed: theory

experimental conditions:

discharge current = 10 mA
$f_c = 140$ MHz
antenna bias relative to anode = -2.2 V

theoretical parameters:

$\theta = 0$ degrees
$l_{oc} = 0.106$ m, $l_{sc} = 0.03$ m
$\rho_{oc} = 0.00026$ m, $\rho_{sc} = 0.0011$ m
probe potential = -3.0321 V
$T_e = 0.2$ eV

$f_p = 793$ MHz
$f_c = 140$ MHz
$f_{uh} = 805$ MHz
$\nu = 500$ MHz
$s = 0.00046031$ m = $12.2075\ \lambda_D$
$\sigma = 3.2127\mathrm{e}{-8}$
o: propagation {abs[real(k_{oc})/imag(k_{oc})] > 20 }
x: cutoff {abs[real(k_{oc})/imag(k_{oc})] < 1 }
+: { 1 < abs[real(k_{oc})/imag(k_{oc})] < 20 }
$f_l = 359$ MHz

Figure 4-10. Field-parallel antenna: theory vs. experiment using $\nu = 500$ MHz which is about 20 times the value used in Fig. 4-9: case with low magnetic field.

damping effect on resonances. Below 1.5 GHz, theoretical predictions qualitatively agree with experiments which are characterized by the appearance of multiple sheath-wave and quarter-wave resonances. Prediction of the position of the quarter-wave resonance is quite accurate. All observed resonances are contained within computed passbands; predicted stopbands are characterized by a lack of identifiable admittance features in the experiments. The frequency f_1 denotes the calculated upper cutoff of the low-frequency passband and well coincides with the point at which the experimental resonances subside into the background. However, the gradual decay with increasing cyclotron frequency of the measured quarter-wave resonance appears

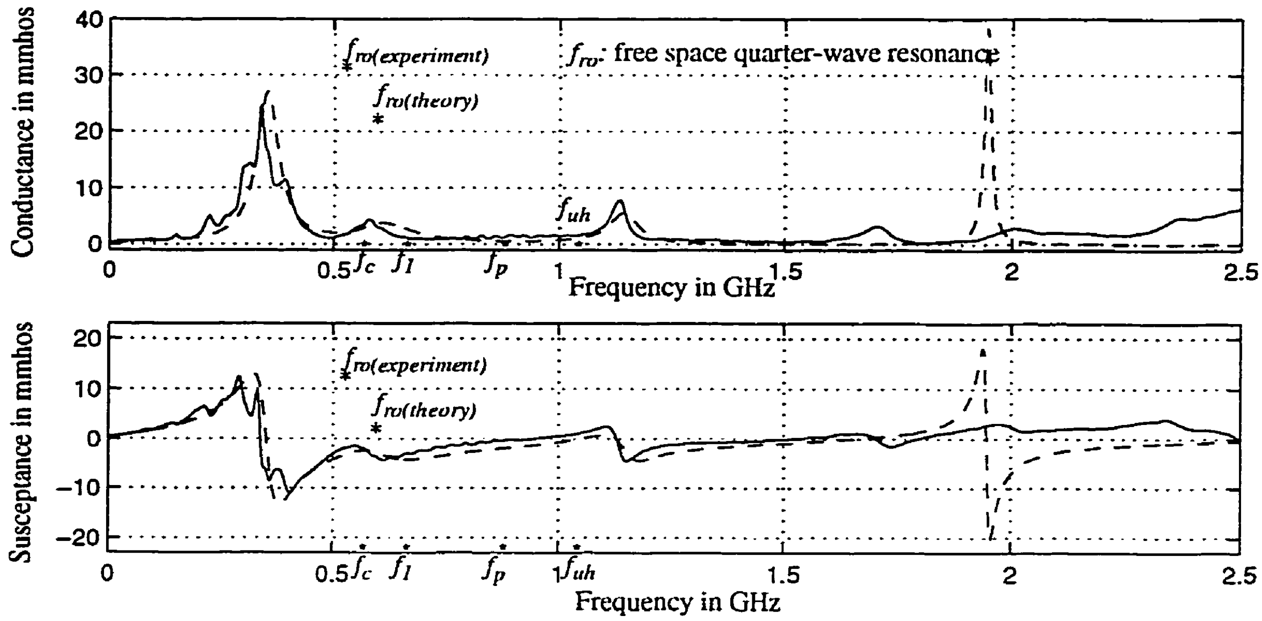

solid: experiment, dashed: theory

experimental conditions:
discharge current = 10 mA
$f_c = 560$ MHz
antenna bias relative to anode = -2.2 V
theoretical parameters:
$\theta = 0$ degrees
$l_{oc} = 0.106$ m, $l_{sc} = 0.03$ m
$\rho_{oc} = 0.00026$ m, $\rho_{sc} = 0.0011$ m
probe potential = -3.0321 V
$T_e = 0.2$ eV

$f_p = 867$ MHz
$f_c = 560$ MHz
$f_{uh} = 1032$ MHz
$\nu = 500$ MHz
$s = 0.00043052$ m = $12.4828\ \lambda_D$
$\sigma = 3.6811\text{e-}8$
o: propagation {abs[real(k_{oc})/imag(k_{oc})] > 20 }
x: cutoff {abs[real(k_{oc})/imag(k_{oc})] < 1 }
+: { 1 < abs[real(k_{oc})/imag(k_{oc})] < 20 }
$f_l = 657$ MHz

Figure 4-11. Field-parallel antenna: comparison of theory with experiment using inflated $\nu = 500$ MHz: case with high magnetic field.

somewhat anomalous since it falls well within the theoretical very-low-attenuation passband (Fig. 4-8 and 4-9). Figure 4-9 illustrates a further comparison for different plasma conditions. Transmission-line theory again exhibits limited accuracy with regard to predicting the exact experimental sheath resonance frequencies. Multiple experimental resonances below 500 MHz are not well-matched by numerically calculated curves. Locations of predicted passbands and stopbands, however, remain consistent with the experimental admittance features.

Variation of collision frequency. The sharp definition of the theoretical curves suggests that inflating the value of the collision frequency beyond that calculated using eq. (2-22) may produce better agreement with the experiment. As an example, in Fig. 4-10 the collision frequency is increased about twenty-fold compared to Fig. 4-8, resulting in much closer resemblance between the curves. This implies that the mechanism of collisional losses may be greater than originally anticipated. Figure 4-11 shows another example supporting the suggestion of inflating the collision frequency which produces rather encouraging agreement between theory and experiment for all frequencies below 1.5 GHz.

Summary. Comparison with the experiments and previous studies leads to the following comments regarding the validity of the transmission-line representation. Modification of the cutoff frequency to a higher value as a result of introducing a finite sheath in the transmission-line calculations is qualitatively consistent with Laurin's work [2]. However, differences arise when quantitative comparisons with Laurin's results are made regarding the actual value of the predicted cutoff frequency, the attenuation level of the low-frequency passband, and the lack of a change in attenuation at f_c. In addition, it was observed that the quarter-wave resonance gradually diminishes with increasing ambient magnetic field, which does not support the prediction of a high-frequency low-attenuation passband. This is to be expected in light of the various crude approximations involved in the derivation of the present model. Nevertheless, its conformity to experimental admittance implies its qualitative usefulness for low-frequency calculations. These observations will facilitate the interpretation of propagation characteristics when analyzing the field-perpendicular antenna.

4.3 Field-Perpendicular Antenna

4.3.1 Theoretical propagation constant

Figure 4-12 depicts the propagation constant for the sheathed and sheathless cases for the

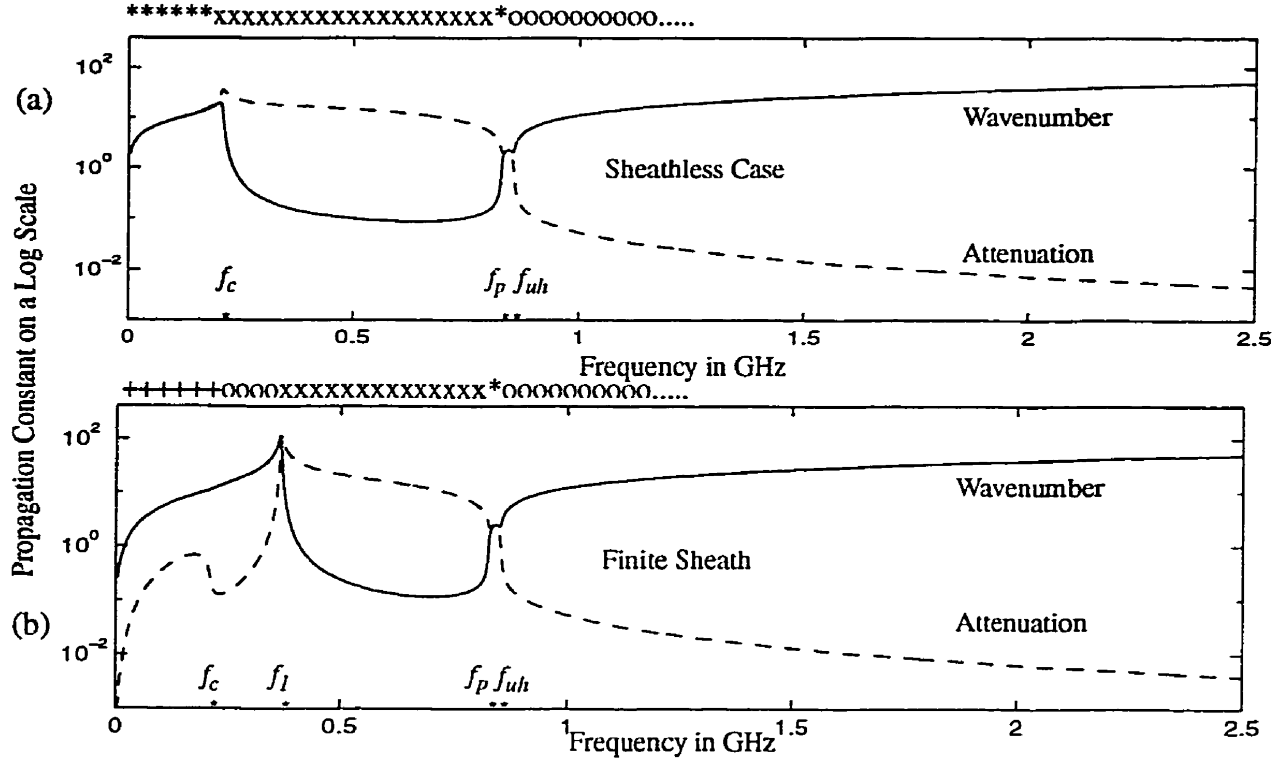

θ = 90 degrees
l_{oc} = 0.106 m
ρ_{oc} = 0.00026 m
ν = 23.3 MHz
f_p = 830 MHz
f_c = 210 MHz
f_{uh} = 856 MHz
a): $s = 0$ m
b): $s = 0.00044484$ m = 12.3475 λ_D

T_e = 0.2 eV
σ = 3.4445e-8
o: propagation {abs[real(k_{oc})/imag(k_{oc})] > 20 }
x: cutoff {abs[real(k_{oc})/imag(k_{oc})] < 1 }
+: { 1 < abs[real(k_{oc})/imag(k_{oc})] < 20 }
*: abs[real(k_{oc})/imag(k_{oc})] = 1
f_l = 375 MHz
solid: imag (k_{oc}) = wavenumber
dashed: real (k_{oc}) = attenuation

Figure 4-12. Field-perpendicular antenna theory: real and imaginary parts of propagation constants for a low ambient magnetic field ($f_c < f_p$).

field-perpendicular antenna. The effect of addition of the finite sheath on the propagation characteristics is apparent from Fig. 4-12 for the case of a moderate ambient magnetic field. In the sheathless case a complex mode (where the absolute values of wavenumber and attenuation are identical) exists up to the cyclotron frequency, followed by a stopband up to the plasma frequency. This is followed by another complex mode up to the upper hybrid frequency and a passband above the upper hybrid frequency. Addition of a sheath results in the occurrence of a low-frequency passband up to a limiting frequency f_l (this frequency would be different from the

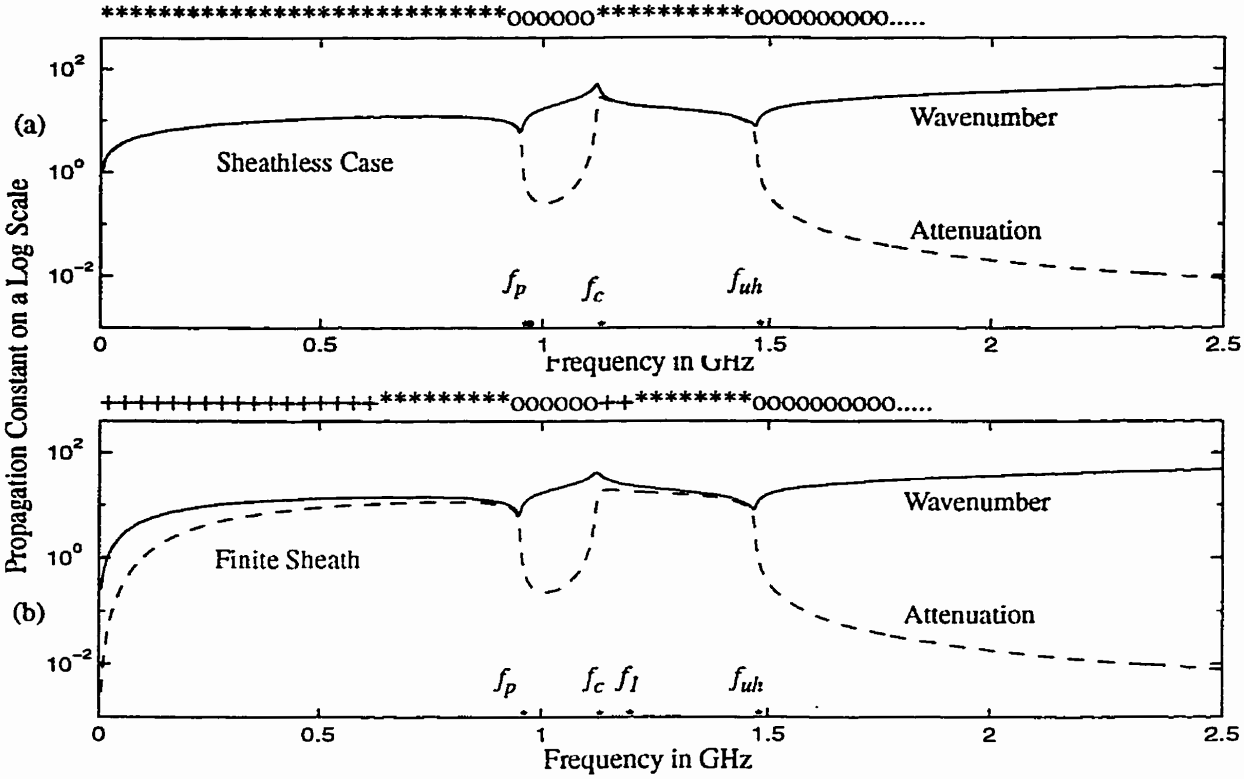

$\theta = 90$ degrees
$l_{oc} = 0.106$ m
$\rho_{oc} = 0.00026$ m
$\nu = 23.3$ MHz
$f_p = 950$ MHz
$f_c = 1120$ MHz
$f_{uh} = 1469$ MHz
a): $s = 0$ m
b): $s = 0.00040199$ m $= 12.7714\ \lambda_D$

$T_e = 0.2$ eV
$\sigma = 4.2287\text{e-}8$
o: propagation {abs[real(k_{oc})/imag(k_{oc})] > 20 }
x: cutoff {abs[real(k_{oc})/imag(k_{oc})] < 1 }
+: { 1 < abs[real(k_{oc})/imag(k_{oc})] < 20 }
*: abs[real(k_{oc})/imag(k_{oc})] = 1
$f_l = 1184$ MHz
solid: imag (k_{oc}) = wavenumber
dashed: real (k_{oc}) = attenuation

Figure 4-13. Field-perpendicular antenna theory: real and imaginary parts of propagation constants for a high ambient magnetic field ($f_c > f_p$).

similarly defined frequency f_l for the field-parallel case). This passband is subdivided into a highly-attenuated passband up to the cyclotron frequency, followed by a very-low-attenuation passband above the cyclotron frequency up to a limiting frequency f_l . Sheath effects therefore are stronger in the perpendicular orientation than for field-parallel antennas with regard to wave propagation along a conductor in a weakly magnetized plasma. On the other hand, for a strong magnetic field, Fig. 4-13 predicts different sheath effects. For the strong ambient magnetic field, the transmission-line calculations suggest virtually identical passband and stopband behaviour above approximately 600 MHz regardless of the existence of a sheath. Below 600 MHz, propagation is facilitated by the introduction of a sheath which reduces the level of attenuation. This high-frequency sheath-independent behaviour is new evidence which has not been observed before, and needs to be experimentally confirmed.

It has been calculated previously in Section 4.2.2 using estimated values that crossing of the cyclotron resonance with the plasma frequency does not affect the propagation characteristics for the field-parallel antenna. For the perpendicular orientation, however, the point at which the cyclotron resonance exceeds the plasma frequency marks a dividing line beyond which the passband behaviour changes significantly. Figure 4-13 illustrates the behaviour of the propagation constant under such circumstances. The predicted low-attenuation high frequency passband between the plasma frequency and the cyclotron frequency as depicted in Fig. 4-13 has also been noted by Adachi [7]. For the sheathless antenna, theory also predicts the existence of a low-attenuation passband between the plasma and the cyclotron frequencies when $f_c > f_p$. Neither of these theoretical findings were verified through experiments due to the limiting coil current generating the ambient magnetic field.

4.3.2 Synopsis by CMA diagrams

To summarize the above observations, the use of CMA diagrams proves helpful. Figure 4-14 depicts all passbands and stopbands as described by the relative magnitude of the real and imaginary parts of the propagation constant. For low ambient magnetic fields, propagation with little attenuation is first encountered as frequency increases along any radial line from DC inwards. A dip in the level of attenuation is predicted (indicated by the change of symbols from + to o) at the cyclotron resonance above which a primary passband ensues, followed by an abrupt

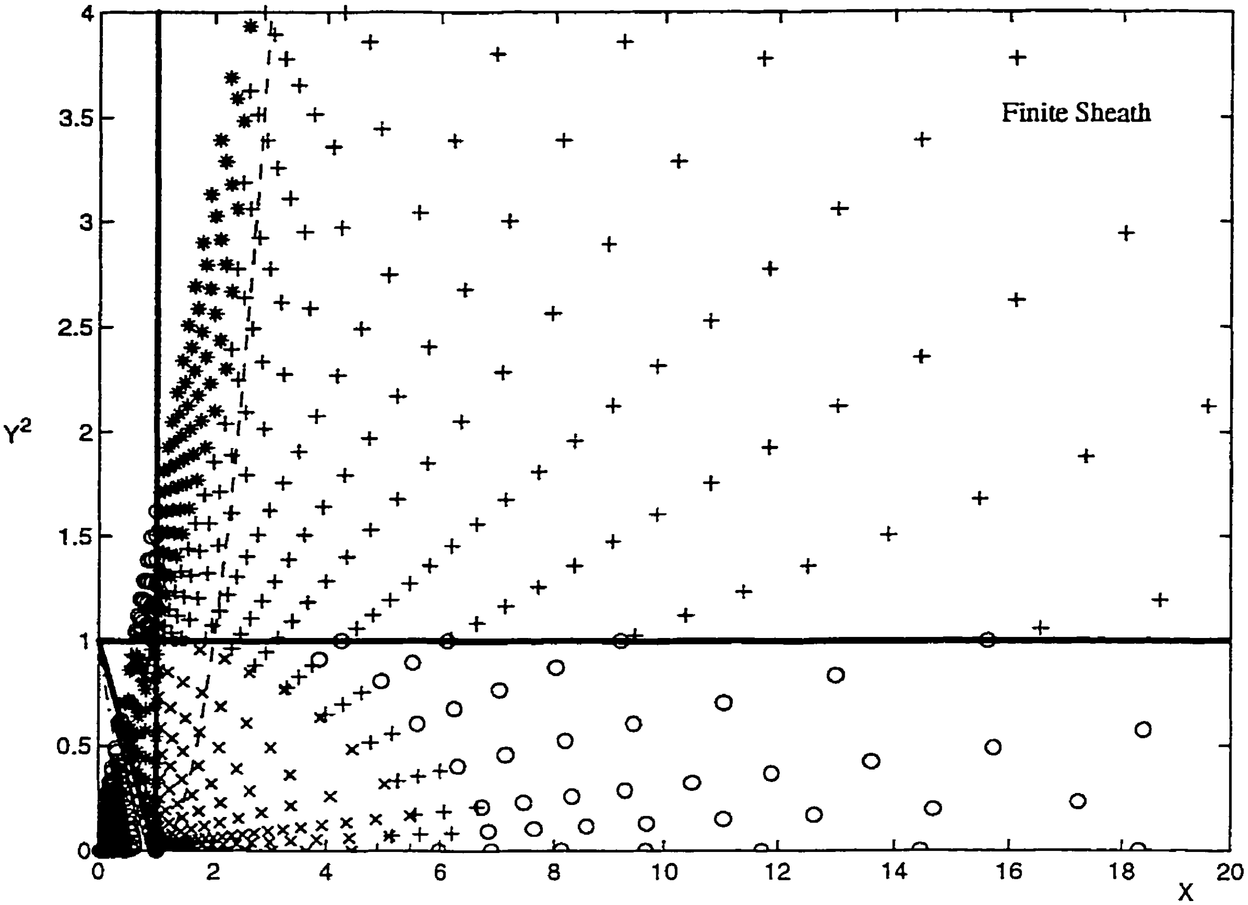

probe potential = -3.0321 V
θ = 90 degrees
v = 23.3 MHz

o: propagation {abs[real(k_{oc})/imag(k_{oc})] > 20 }
x: cutoff {abs[real(k_{oc})/imag(k_{oc})] < 1 }
+: attenuated propagation {1< abs[real(k_{oc})/imag(k_{oc})] < 20 }
*: complex mode {abs[real(k_{oc})/imag(k_{oc})] = 1 }

Figure 4-14. Field-perpendicular antenna: theoretical propagation characteristics displayed on a CMA diagram for the sheathed case.

transition into a stopband. The plasma frequency marks the onset of the complex mode, extending up to the upper hybrid frequency beyond which propagation resumes with little attenuation. In situations where the cyclotron frequency becomes comparable to the plasma frequency, the aforementioned low-attenuation passband becomes narrower and eventually vanishes, being replaced by more highly attenuated propagation. Lowering of the upper threshold of the primary passband as a result of reducing sheath thickness translates into an outward shift of the low frequency, low-attenuation passband on the CMA diagram, indicating a narrower

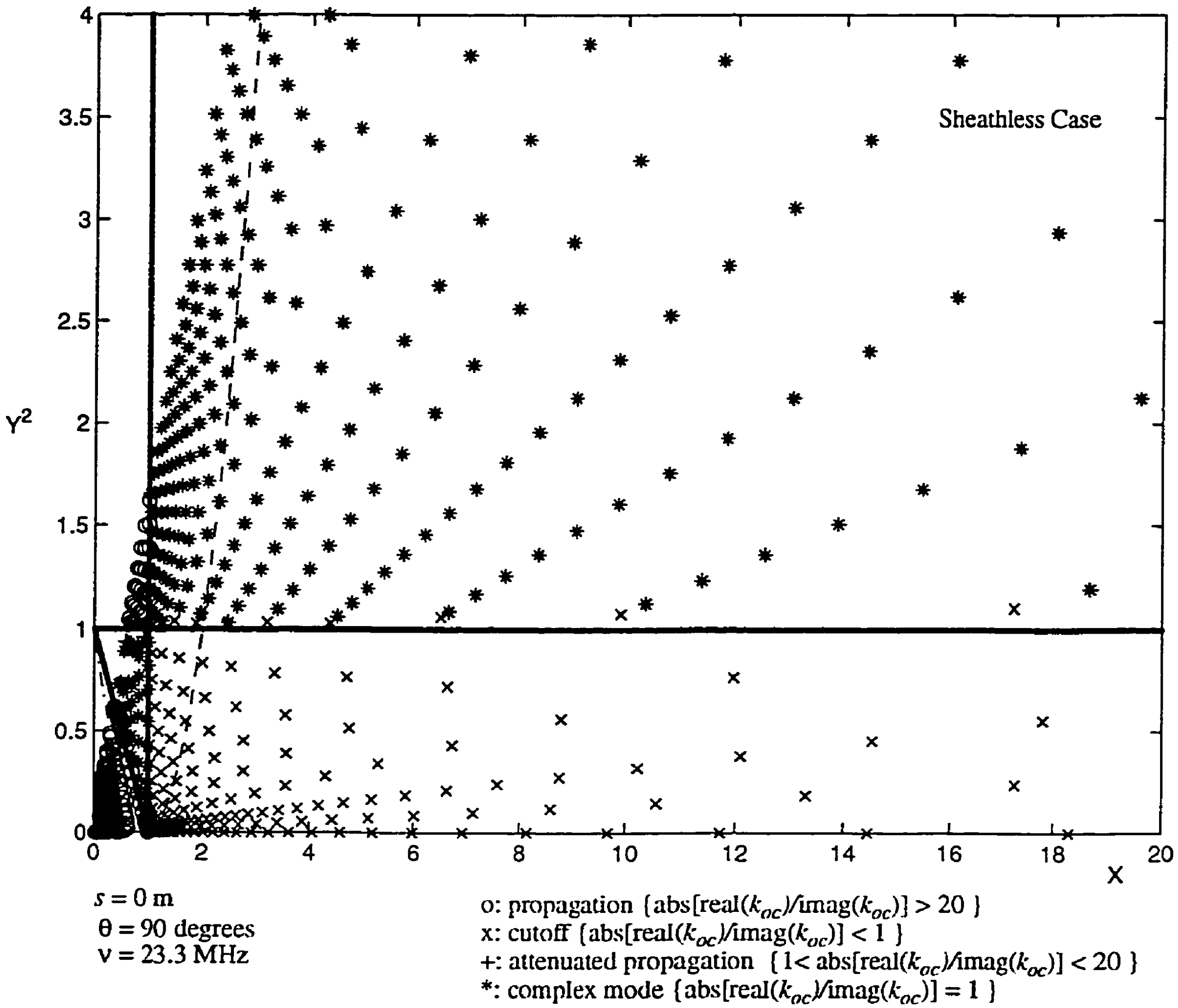

Figure 4-15. Field-perpendicular antenna: CMA diagram for the sheathless case.

frequency range available for weakly-attenuated propagation. In the limiting case of sheath reduction to zero thickness, this passband region indicated by circles is completely absent as in Fig. 4-15. Variation in collision frequency, on the other hand, has no influence on the propagation characteristics other than slightly modifying the frequencies at which passband-stopband transitions occur.

Figure 4-15 presents overall propagation characteristics for the field-perpendicular antenna in the absence of a sheath along the wire. Low-frequency behaviour is characterized by a complex mode from DC up to the cyclotron frequency where transition into a stopband occurs. Cutoff conditions continue until reaching the plasma frequency. Characteristics of the stopbands and passbands above the plasma frequency for the sheathless situation remain identical to the sheathed calculations in Fig. 4-14 . A summary of the critical frequencies for sheath resonance passbands is presented in Tables 4-1 through 4-3 for antennas with parallel or perpendicular orientation with respect to the ambient magnetic field.

Table 4-1 Calculated Passbands and Stopbands for Field-Parallel Antenna

no sheath	low-attenuation passband from DC to f_c	stopband between f_c and f_{uh}	low-attenuation passband above f_{uh}
finite sheath	low-attenuation passband from DC to f_l	stopband between f_l and f_{uh}	low-attenuation passband above f_{uh}

Table 4-2 Calculated Passbands and Stopbands for Field-Perpendicular Antenna: $f_p > f_c$

no sheath	complex mode from DC to f_c	stopband from f_c to f_p	complex mode from f_p to f_{uh}	low-attenuation passband above f_{uh}	
finite sheath	atteunated propagation from DC to f_c	low-attenuation passband from f_c to f_l	stopband from f_l to f_p	complex mode from f_p to f_{uh}	low-attenuation passband above f_{uh}

Table 4-3 Calculated Passbands and Stopbands for Field-Perpendicular Antenna: $f_p < f_c$

no sheath	complex mode from DC to f_p	low-attenuation passband from f_p to f_c	complex mode from f_c to f_{uh}	low-attenuation passband above f_{uh}
finite sheath	attenuated propagation from DC to f_p	low-attenuation passband from f_p to f_c	complex mode from f_c to f_{uh}	low-attenuation passband above f_{uh}

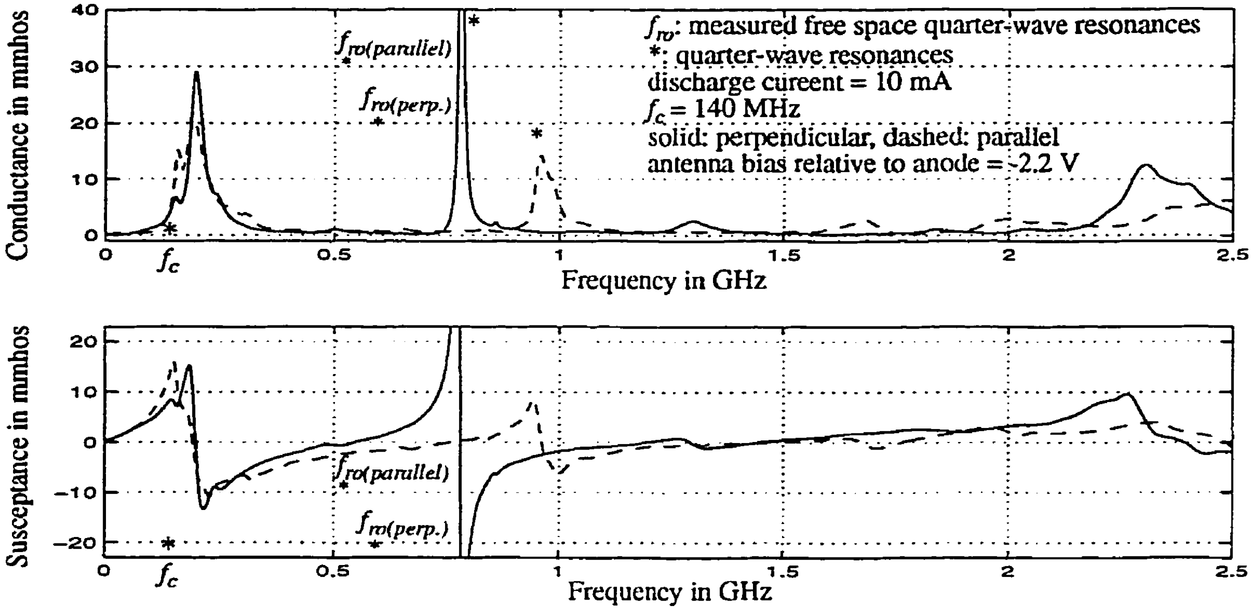

Figure 4-16. Influence of antenna orientation on experimental quarter-wave resonances.

4.3.3 Observation of admittance

Quarter-wave resonance. A distinct feature of experimental admittance data is the very narrow bandwidth and high magnitude of the quarter-wave resonance. Figure 4-16 provides a clear contrast in relative magnitude of the respective quarter-wave resonances of the two antennas. The resonance peak of the antenna of interest is much more emphasized than that of the field-parallel monopole. This is speculated to be a consequence of the parallel orientation of the monopole with respect to the ground plane. This particular physical arrangement along with its image more closely resembles the construction of a transmission line, thus resulting in lower radiation losses by the antenna.

Another observation is the difference in frequencies of the quarter-wave resonance between field-parallel and field-perpendicular antennas. The field-perpendicular monopole exhibits resonance frequencies that are up to 25% lower than its field-parallel counterpart as indicated in Fig. 4-16. A plausible explanation considers the relevant plasma permittivity for each

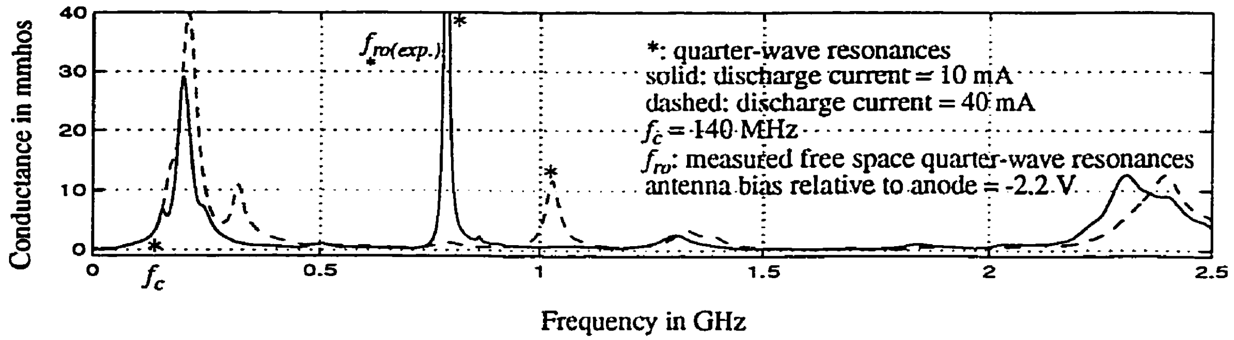

Figure 4-17. Field-perpendicular antenna experiments: influence of discharge current on quarter-wave resonance.

physical arrangement. It is known that the resonance frequency of an antenna is directly related to the specific medium permittivity. Because of the medium anisotropy, calculation of the field-perpendicular effective permittivity requires contributions from elements K_0 and K' of the dielectric tensor, thus giving rise to a quarter-wave resonance frequency different from that of the parallel antenna whose relevant permittivity is given by K'.

The influence of variation in discharge current on the strength of the resonance is illustrated in Fig. 4-17 which shows the relative magnitude of the quarter-wave resonance at two different discharge currents. The effect of the increase in the plasma density is an upshift in frequency of the resonance and its diminishing with the ambient magnetic field.

Sheath wave resonances: characterization by bias and magnetic field variation. The data of Fig. 4-18 for the field-perpendicular antenna at low cyclotron frequencies reveals that admittance variation with frequency below 500 MHz is dominated by admittance maxima. Bias dependence of these low frequency resonances is especially pronounced at low cyclotron frequencies. For comparison purposes, the data in Fig. 4-18 were taken under identical laboratory conditions with the exception of switching from negative to positive bias. It was observed that with the collapse of the sheath, low frequency resonance features have been strongly suppressed.

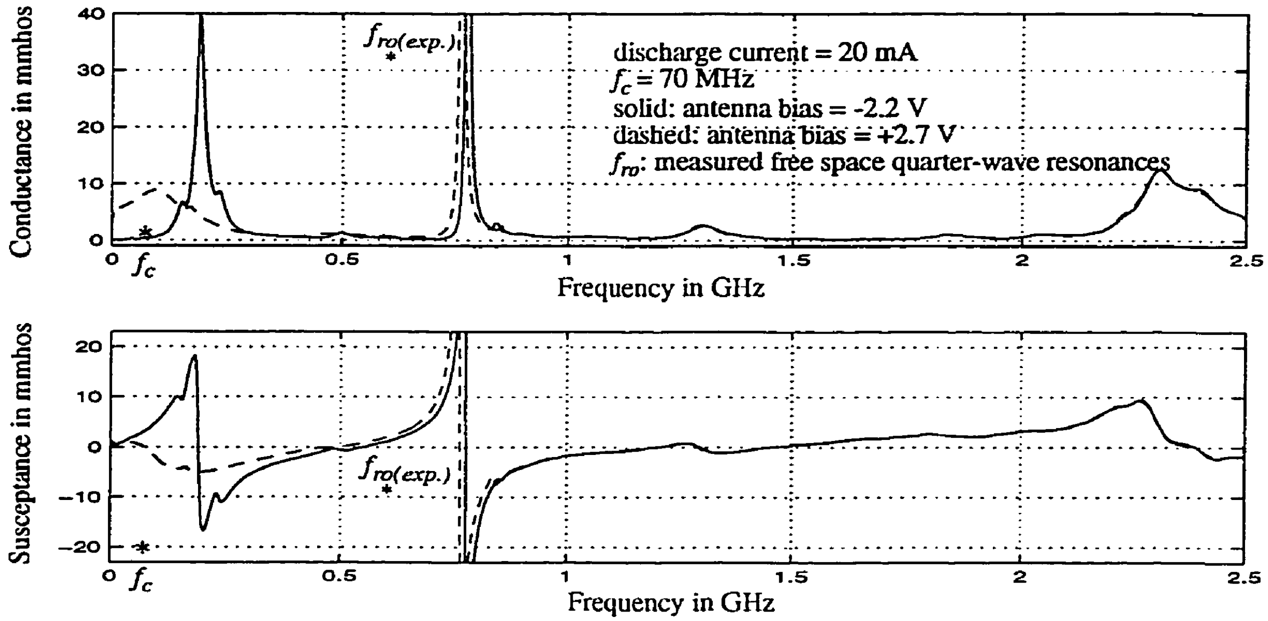

Figure 4-18. Field-perpendicular antenna experiments: low-frequency dependence of admittance on applied bias.

An additional factor conducive to the identification of these resonances as sheath wave effects is the observation that the frequency range of these resonances corresponds to plasma conditions of cutoff for all modes of plane waves. Thus this combination of evidence suggests the existence of a low frequency, low-attenuation passband available for sheath wave propagation in the presence of a weak ambient magnetic field. This passband appears to be restricted in a low-frequency region just as predicted by theory which calculates the upper cutoff to be frequency f_l, the point at which the magnitude of the attenuation becomes higher than that of the wavenumber. These sheath waves are strictly contained below 500 MHz.

Figure 4-19 depicts successive measurements taken with increasing cyclotron frequency. It is observed that as the cyclotron frequency moves up in frequency through the admittance peaks, the sheath wave resonance broadens considerably. This broadening effect becomes even more pronounced with further increase in the ambient magnetic field. This behaviour therefore suggests the lower cutoff for the passband to be the cyclotron frequency. This is well supported

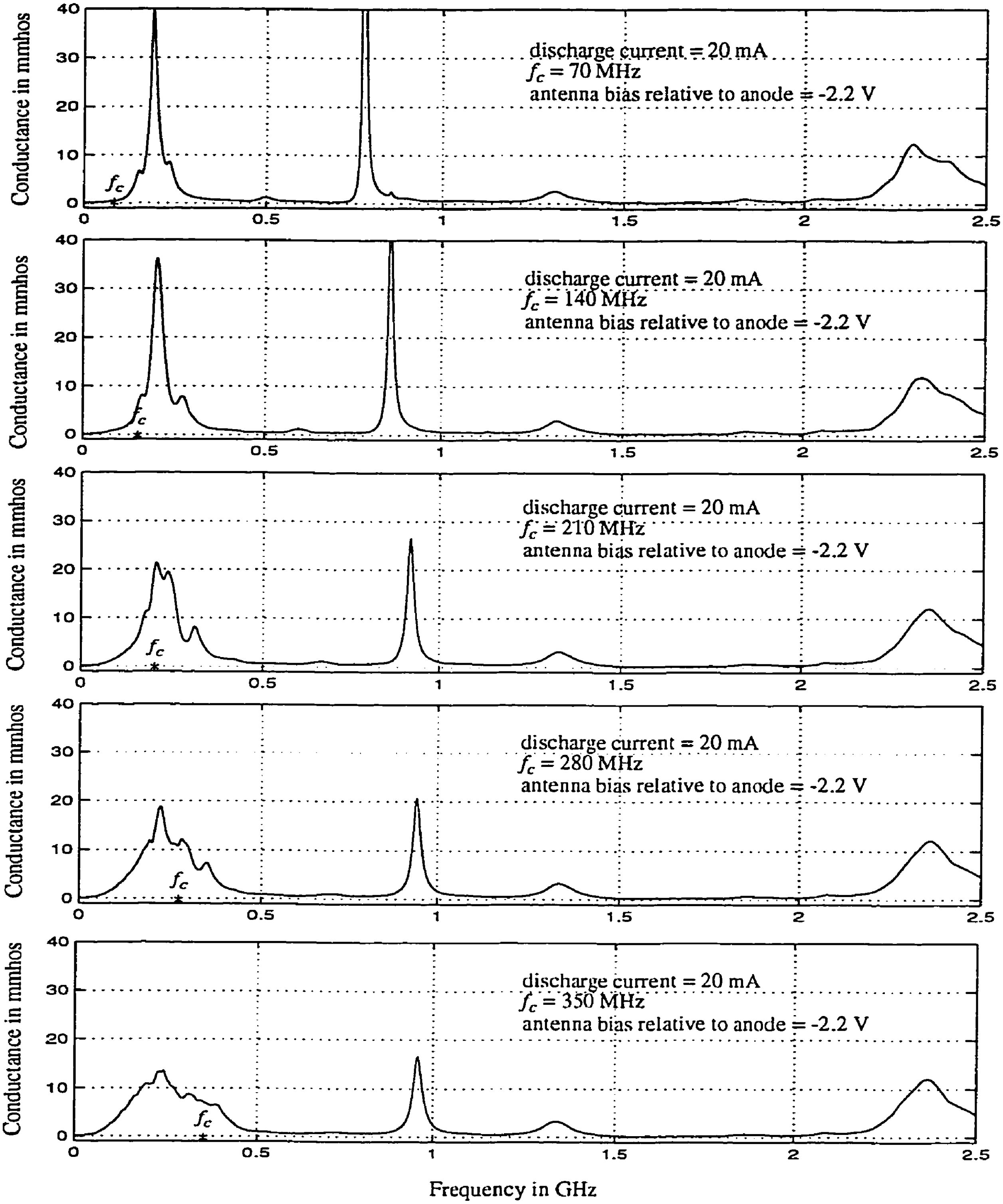

Figure 4-19. Field-perpendicular antenna: evolution of experimental sheath wave resonances with increasing ambient magnetic field.

by the theoretical calculations of Fig. 4-12 which predict an abrupt decrease in the attenuation

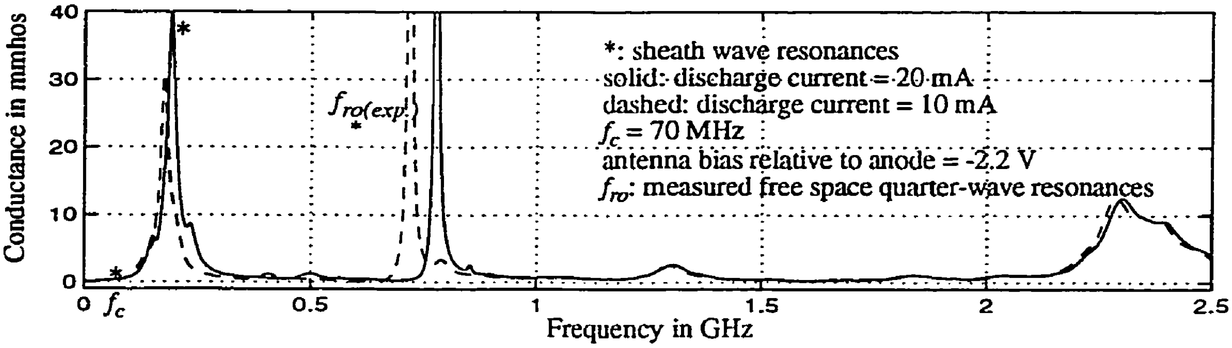

Figure 4-20. Field-perpendicular antenna experiments: influence of discharge current on quarter-wave resonance.

level at the cyclotron frequency, resulting in a low-attenuation frequency range becoming available for sheath wave propagation. It is interesting to note in Fig. 4-16 that sheath resonances for both antennas occur at identical frequencies in the presence of a weak ambient magnetic field. This observation may warrant further attention in the future.

Figure 4-20 compares the sheath wave resonances observed at two discharge currents with little difference although the quarter-wave resonance has been shifted appreciably. Variation in the discharge current does not alter the essential characteristics of the sheath wave resonances although their magnitude has been enhanced by increasing the plasma discharge current. Variation in negative bias setting, on the other hand, sees reinforcement of one single conductance maximum for more negative antenna bias, as well as resonance-splitting for less negative bias, as

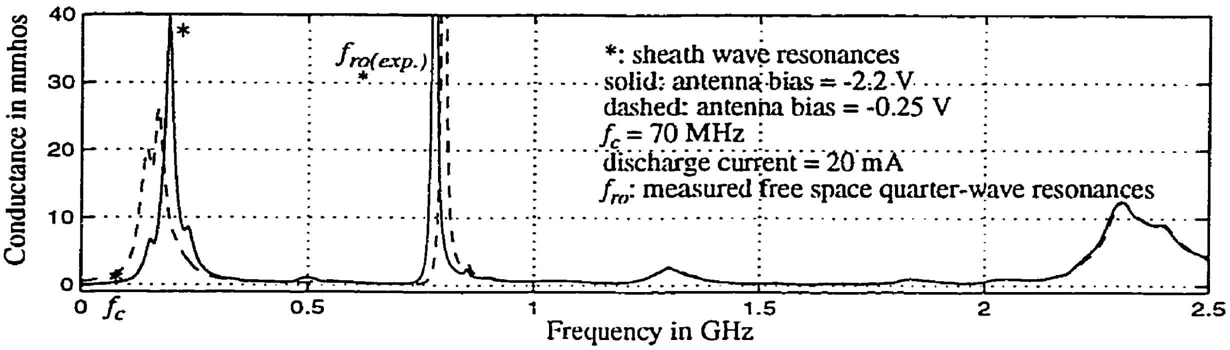

Figure 4-21. Field-perpendicular antenna experiments: influence of applied bias on admittance.

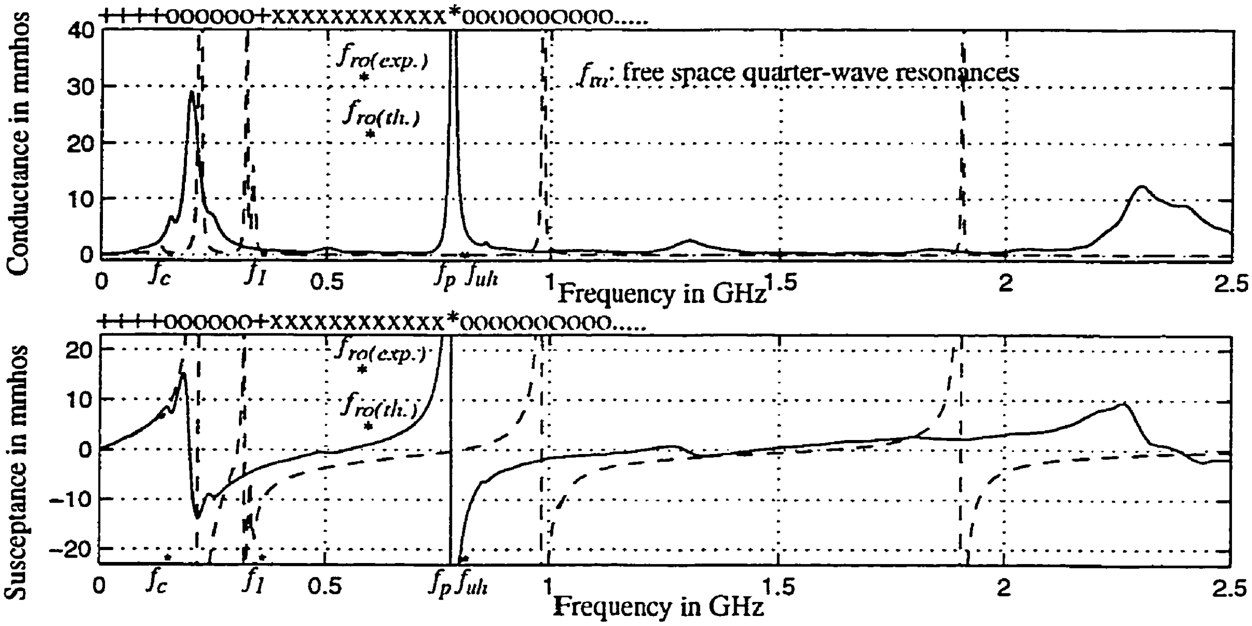

solid: experiment, dashed: theory

experimental conditions:
discharge current = 10 mA
f_c = 140 MHz
antenna bias relative to anode = -2.2 V
theoretical parameters:
θ_{oc} = 90 degrees
θ_{sc} = 0 degrees
l_{oc} = 0.106 m, l_{sc} = 0.03 m
ρ_{oc} = 0.00026 m, ρ_{sc} = 0.0011 m
probe potential = -3.0321 V
T_e = 0.2 eV

f_p = 793 MHz
f_c = 140 MHz
f_{uh} = 805 MHz
ν = 23.3 MHz
s = 0.00046031 m = 12.2075 λ_D
σ = 3.2127e-8
o: propagation {abs[real(k_{oc})/imag(k_{oc})] > 20 }
x: cutoff {abs[real(k_{oc})/imag(k_{oc})] < 1 }
+: { 1 < abs[real(k_{oc})/imag(k_{oc})] < 20 }
*: abs[real(k_{oc})/imag(k_{oc})] = 1
f_l = 350 MHz

Figure 4-22. Field-perpendicular antenna: theoretical vs. experimental admittance for low ambient magnetic field.

indicated in Fig. 4-21. Resonance frequencies are also observed to undergo a slight upward shift with increasingly negative bias.

4.3.4 Comparison with transmission line calculations

Admittance calculations for the field-parallel antenna reveal some limitations inherent in the transmission-line approach. These are manifested in two aspects: 1) calculations of sheath wave resonance frequencies are prone to be inaccurate, and 2) departure of theory from experiment at high frequencies. These observations become useful when analyzing the field-perpendicular antenna.

Experimental vs. theoretical admittance: passbands and stopbands. Figure 4-22 is an example of experimental admittance variation with frequency on which theoretical computations are superposed. This particular set of results corresponds to an experimental antenna bias setting of -2.2V relative to the anode potential. As in the case of the field-parallel antenna, experimental admittance behaviour at high frequencies eludes the interpretation based on transmission-line analysis. Some agreement is obtained for the low-frequency passband below 500 MHz, characterized by several well-defined conductance maxima. The sharp definition of the computed quarter-wave resonance is mirrored by the very low bandwidth of its experimental counterpart, although the resonance frequency is not well predicted. Figure 4-22 also depicts the location of predicted passbands and stopbands relative to the experimental admittance features. For various plasma conditions, theory mostly predicts either a complex mode (defined by equal magnitude of the real and imaginary parts of the propagation constant) or a stopband at the location of the experimental quarter-wave resonance. Given the magnitude of the observed quarter-wave resonance suggestive of very low attenuation, it is evident that the transmission-line model fails to predict accurately the position of the stopband. This is not surprising realizing the high frequency limitations of the transmission-line theory as applied to the analysis of approximate TM mode sheath waves. The presence of an experimental "hump" just below the cyclotron frequency is constant throughout the entire range of plasma conditions encountered in the experiment and is paralleled by theoretical calculations of a low admittance peak at the cyclotron frequency. Figure 4-23 provides another comparison between the resonance maxima and the location of the predicted passband at slightly higher plasma and cyclotron frequencies. It should be emphasized

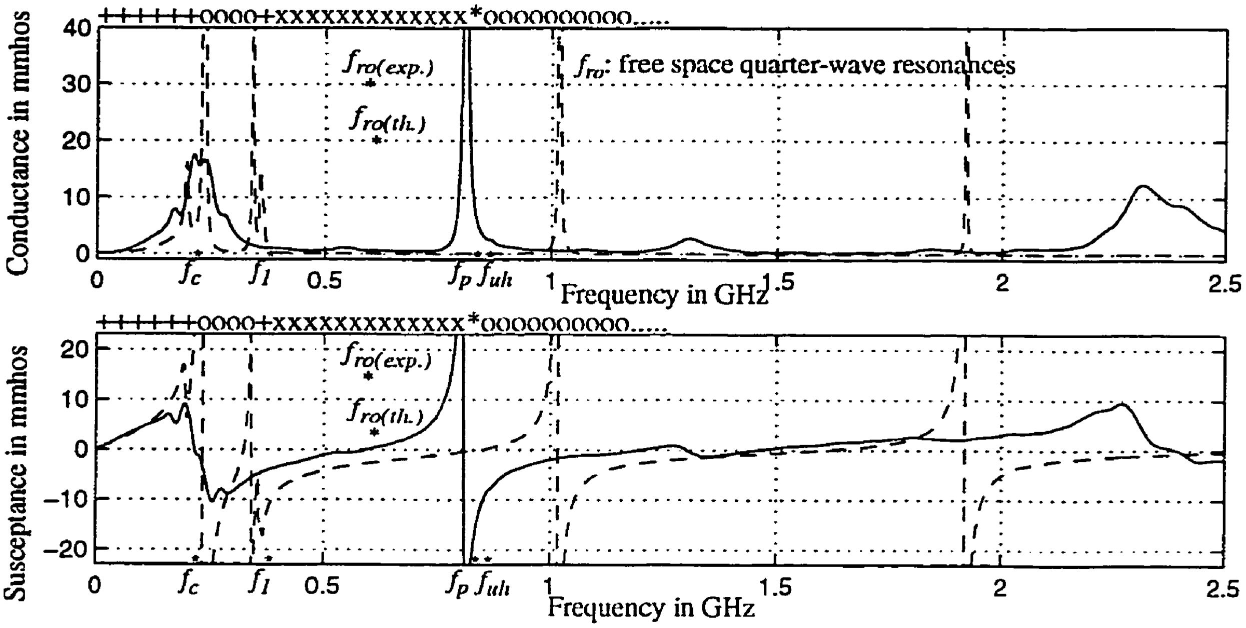

solid: experiment, dashed: theory

experimental conditions:

discharge current = 10 mA
f_c = 210 MHz
antenna bias relative to anode = -2.2 V

theoretical parameters:

θ_{oc} = 90 degrees
θ_{sc} = 0 degrees
l_{oc} = 0.106 m, l_{sc} = 0.03 m
ρ_{oc} = 0.00026 m, ρ_{sc} = 0.0011 m
probe potential = -3.0321 V
T_e = 0.2 eV

f_p = 830 MHz
f_c = 210 MHz
f_{uh} = 856 MHz
ν = 23.3 MHz
s = 0.00044484 m = 12.3475 λ_D
σ = 3.4445e-8
o: propagation {abs[real(k_{oc})/imag(k_{oc})] > 20 }
x: cutoff {abs[real(k_{oc})/imag(k_{oc})] < 1 }
+: { 1 < abs[real(k_{oc})/imag(k_{oc})] < 20 }
*: abs[real(k_{oc})/imag(k_{oc})] = 1
f_l = 375 MHz

Figure 4-23. Field-perpendicular antenna: theory vs. experiment for moderate ambient magnetic field.

that observation of these resonances is limited to situations in which the ambient magnetic field is weak.

A characteristic evident from theoretical computations is the broadening effect of increasing magnetic field on the sheath wave resonance group. Figure 4-24 shows that the experimental resonances behave exactly in this broadening pattern with increasing cyclotron frequency as predicted, with the admittance turning into a plateau at low frequencies.

Variation of collision frequency. It has been suggested previously that the theoretical

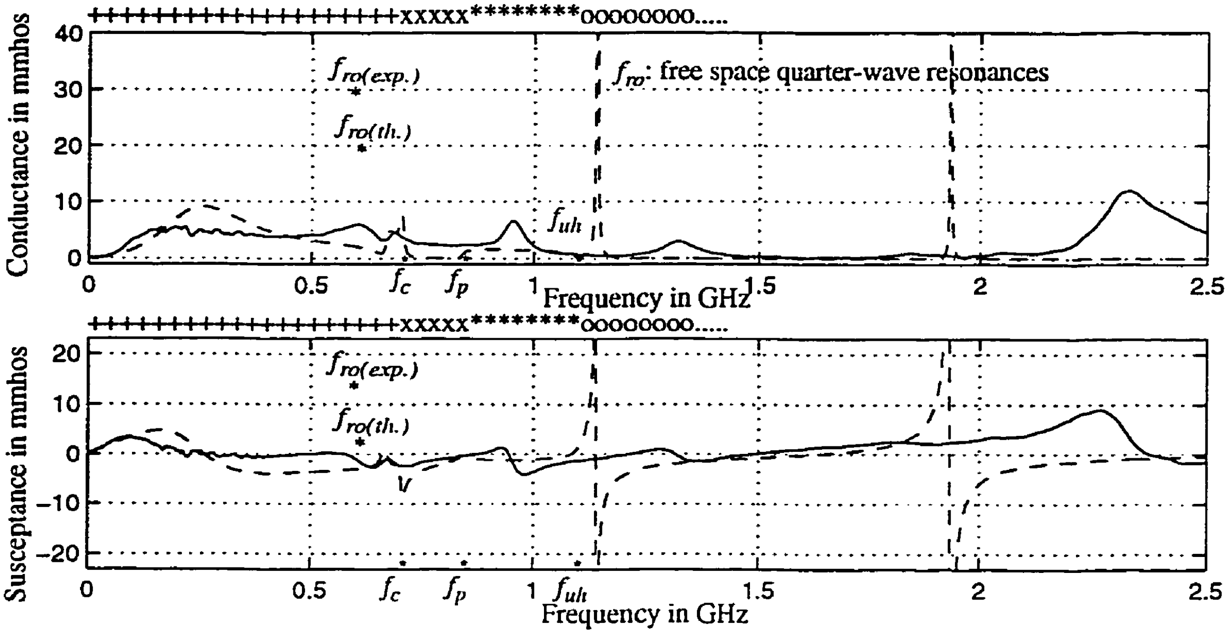

solid: experiment, dashed: theory

experimental conditions:
discharge current = 10 mA
$f_c = 700$ MHz
antenna bias relative to anode = -2.2 V
theoretical parameters:
$\theta_{oc} = 90$ degrees
$\theta_{sc} = 0$ degrees
$l_{oc} = 0.106$ m, $l_{sc} = 0.03$ m
$\rho_{oc} = 0.00026$ m, $\rho_{sc} = 0.0011$ m
probe potential = -3.0321 V
$T_e = 0.2$ eV

$f_p = 836$ MHz
$f_c = 700$ MHz
$f_{uh} = 1090$ MHz
$\nu = 23.3$ MHz
$s = 0.00044244$ m = 12.3697 λ_D
$\sigma = 3.4826\text{e-}8$
o: propagation {abs[real(k_{oc})/imag(k_{oc})] > 20 }
x: cutoff {abs[real(k_{oc})/imag(k_{oc})] < 1 }
+: { 1 < abs[real(k_{oc})/imag(k_{oc})] < 20 }
*: abs[real(k_{oc})/imag(k_{oc})] = 1

Figure 4-24. Field-perpendicular antenna: experiment/theory comparison showing resonance broadening effect of strong ambient magnetic field.

collision frequency may be somewhat lower than its actual value, evidenced by the narrow bandwidth of the experimental resonance maxima. Therefore, in Fig. 4-25 a highly inflated collision frequency is introduced to calculate its influence on the admittance data. Figure 4-25 illustrates the damping effect of a magnified collision frequency on the resonance, resulting in closer resemblance between theory and experiment compared with Fig. 4-22. Below the quarter-wave resonance, predicted passbands and stopbands are well matched by experimental conductance features of maxima and plains of minima. Fig. 4-26 is another comparison using an

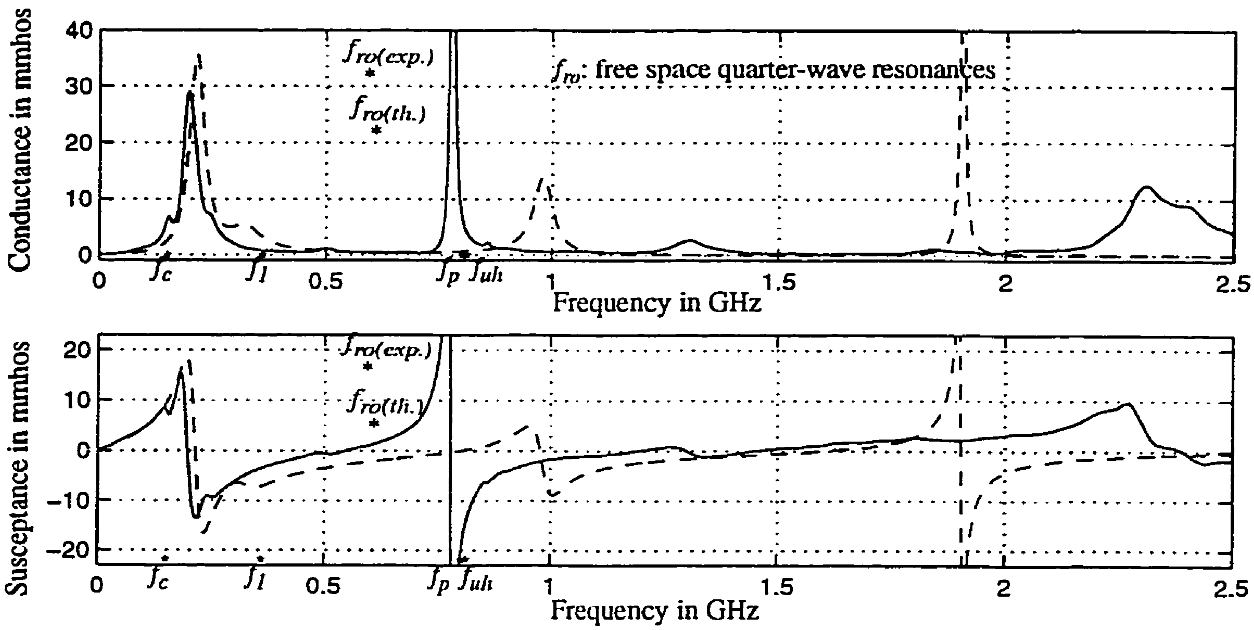

solid: experiment, dashed: theory

experimental conditions:
discharge current = 10 mA
f_c = 140 MHz
antenna bias relative to anode = -2.2 V
theoretical parameters:
θ_{oc} = 90 degrees
θ_{sc} = 0 degrees
l_{oc} = 0.106 m, l_{sc} = 0.03 m
ρ_{oc} = 0.00026 m, ρ_{sc} = 0.0011 m
probe potential = -3.0321 V
T_e = 0.2 eV

f_p = 793 MHz
f_c = 140 MHz
f_{uh} = 805 MHz
ν = 500 MHz
s = 0.00046031 m = 12.2075 λ_D
σ = 3.2127e-8
o: propagation {abs[real(k_{oc})/imag(k_{oc})] > 20 }
x: cutoff {abs[real(k_{oc})/imag(k_{oc})] < 1 }
+: { 1 < abs[real(k_{oc})/imag(k_{oc})] < 20 }
*: abs[real(k_{oc})/imag(k_{oc})] = 1
f_l = 350 MHz

Figure 4-25. Field-perpendicular antenna: comparison of theory with experiment using inflated ν = 500 MHz, for a low ambient magnetic field.

exaggerated collision frequency in the calculations which leads to partial overlapping of the low frequency resonances from theory and experiment.

Influence of sheath conductivity. A previous discussion of effective sheath conductivity indicates that neglecting the magnetic field action results in estimates of conductivity somewhat higher than the actual effective value. Figure 4-27 illustrates a comparison of admittance calculated using conductivity determined by eq. (2-16) with the result computed using a hundred-fold reduced conductivity. The reduction is observed to produce virtually identical

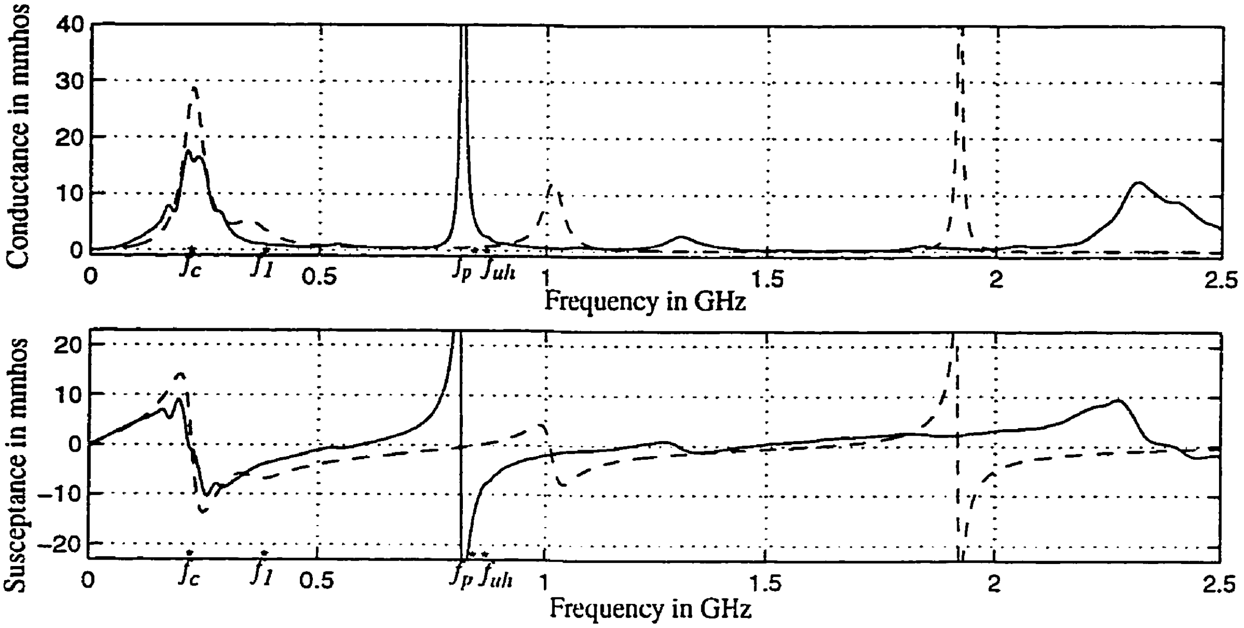

solid: experiment, dashed: theory

experimental conditions:
discharge current = 10 mA
$f_c = 210$ MHz
antenna bias relative to anode = -2.2 V
theoretical parameters:
$\theta_{oc} = 90$ degrees
$\theta_{sc} = 0$ degrees
$l_{oc} = 0.106$ m, $l_{sc} = 0.03$ m
$\rho_{oc} = 0.00026$ m, $\rho_{sc} = 0.0011$ m
probe potential = -3.0321 V
$T_e = 0.2$ eV

$f_p = 830$ MHz
$f_c = 210$ MHz
$f_{uh} = 856$ MHz
$\nu = 500$ MHz
$s = 0.00044484$ m $= 12.3475\ \lambda_D$
$\sigma = 3.4445\text{e-}8$
o: propagation {abs[real(k_{oc})/imag(k_{oc})] > 20 }
x: cutoff {abs[real(k_{oc})/imag(k_{oc})] < 1 }
+: { 1 < abs[real(k_{oc})/imag(k_{oc})] < 20 }
*: abs[real(k_{oc})/imag(k_{oc})] = 1
$f_l = 375$ MHz

Figure 4-26. Field-perpendicular antenna: comparison of theory with experiment using inflated collision frequency for moderate ambient magnetic field.

admittance data, thus its effect is likely to be inconsequential when calculating resonance frequencies.

Variation of sheath thickness. One other aspect of theoretical calculations which warrants mentioning is the variation of sheath thickness implemented numerically. Figure 4-28 depicts a comparision of experimental admittance with theoretical results for an intermediate negative bias setting of -0.25V (between the experimental positive and negative bias extremes of +2.7V and -2.2V). This corresponds to a sheath thickness reduction to roughly 7 Debye lengths.

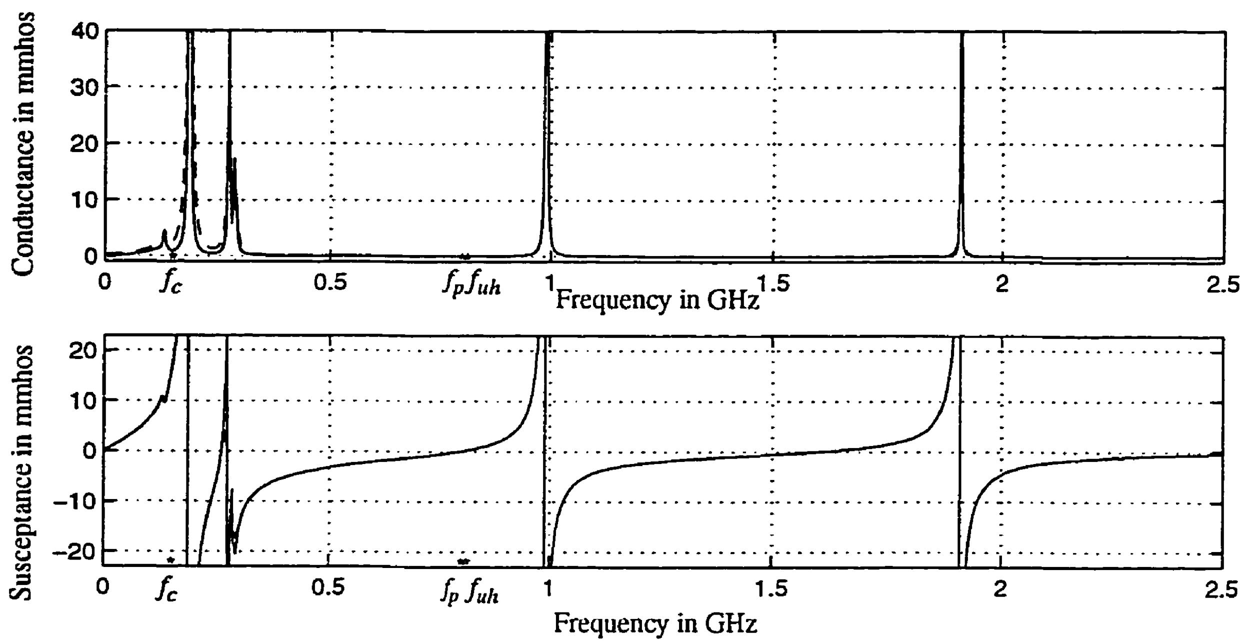

$\theta_{oc} = 90$ degrees
$\theta_{sc} = 0$ degrees
$l_{oc} = 0.106$ m, $l_{sc} = 0.03$ m
$\rho_{oc} = 0.00026$ m, $\rho_{sc} = 0.0011$ m
probe potential = -1.0821 V
$T_e = 0.2$ eV

$f_p = 793$ MHz
$f_c = 140$ MHz
$f_{uh} = 805$ MHz
$\nu = 23.3$ MHz
$s = 0.00027499$ m $= 7.2926\ \lambda_D$
dashed: $\sigma = 3.9025e\text{-}4$
solid: $\sigma = 3.9025e\text{-}6$

Figure 4-27. Field-perpendicular antenna theory: effect of varying sheath conductivity on admittance.

The extent to which theory agrees with experiment remains limited to the low frequency region in which resonances are observed. The only observable effect as a result of the reduction in sheath thickness in the computations is a slight downshift of the upper cutoff of the low-attenuation sheath resonance passband. Further decrease in sheath thickness restricts the passband to an even more limited frequency range above cyclotron resonance. Properties of high frequency propagation remain unchanged as one would expect since sheath variation is a low frequency characteristic regardless of the antenna orientation. Characteristics for the extreme case of sheath collapse are displayed using CMA diagram in Fig. 4-15.

Summary. The most substantial insight from the present analysis is the discovery of a

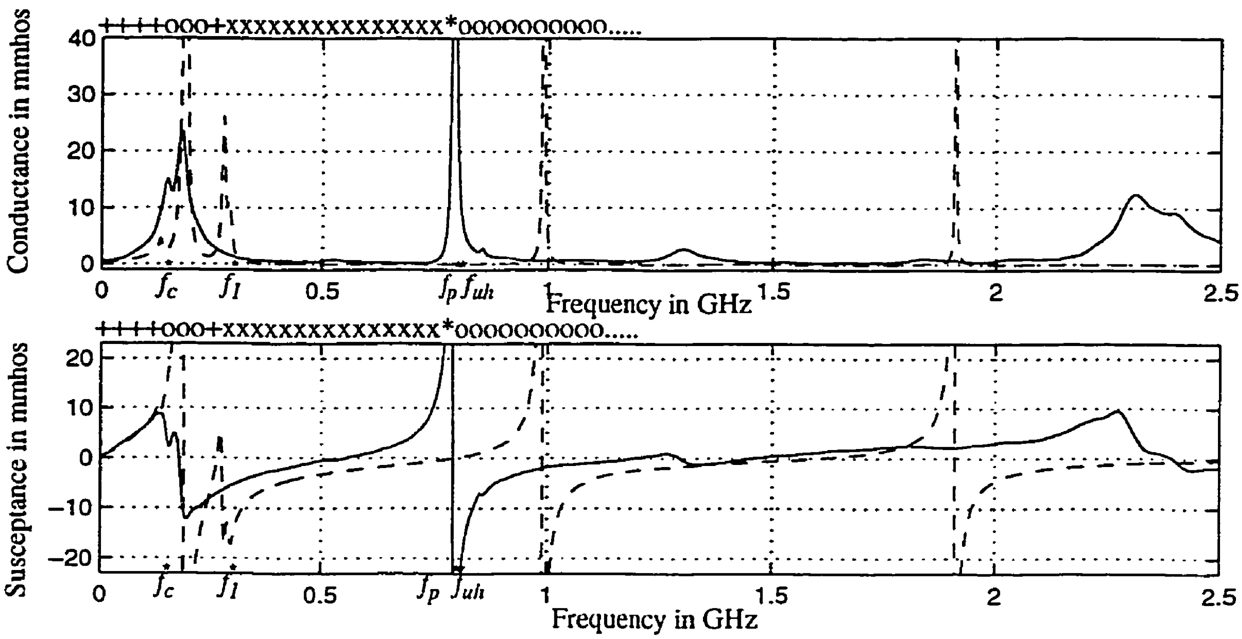

solid: experiment, dashed: theory

experimental conditions:

discharge current = 10 mA
f_c = 140 MHz
antenna bias relative to anode = -0.25 V

theoretical parameters:

θ_{oc} = 90 degrees
θ_{sc} = 0 degrees
l_{oc} = 0.106 m, l_{sc} = 0.03 m
ρ_{oc} = 0.00026 m, ρ_{sc} = 0.0011 m
probe potential = -1.0821 V
T_e = 0.2 eV

f_p = 793 MHz
f_c = 140 MHz
f_{uh} = 805 MHz
ν = 23.3 MHz
s = 0.00027499 m = 7.2926 λ_D
σ = 3.9025e-4
o: propagation {abs[real(k_{oc})/imag(k_{oc})] > 20 }
x: cutoff {abs[real(k_{oc})/imag(k_{oc})] < 1 }
+: { 1 < abs[real(k_{oc})/imag(k_{oc})] < 20 }
*: abs[real(k_{oc})/imag(k_{oc})] = 1
f_l = 289 MHz

Figure 4-28. Field-perpendicular antenna: experiment/theory comparison for a lower applied bias producing a thinner sheath compared with Fig. 4-22.

low frequency, low-attenuation sheath wave passband bounded below by the cyclotron frequency. Transmission-line theory has predicted its existence as discussed in the previous section, and it has been confirmed by experimental observation. The upper limit of this numerically calculated passband, denoted f_l, does not relate to familiar plasma parameters. It is interesting to compare this with a previous study by Baker [3] which revealed the existence of a passband between the cyclotron resonance and $\frac{f_{uh}}{\sqrt{2}}$ for propagation of sheath waves on a field-perpendicular planar conductor. The lower cutoff coincides with Baker's prediction, but the upper limit is different from $\frac{f_{uh}}{\sqrt{2}}$. Further, the level of attenuation in the passband predicted by the transmission-line model is lower than that of Baker's results. This is not surprising because the orientation of the ambient magnetic field in the present study changes around the circumference of the antenna surface and therefore calculating its impedance becomes a more complicated task. In comparison, Baker's analysis involves a perpendicular orientation of the ambient magnetic field that remains constant over the conductor surface.

Chapter 5

CONCLUSIONS

Laboratory measurement of antenna admittance was conducted emphasizing the low frequency range appropriate for the observation of sheath wave passbands for a cylindrical conductor oriented perpendicular to the ambient magnetic field. A transmission-line theory for plasma-immersed structures was modified to take the ion sheath into account, and to enable comparison with experimental admittance results. The computational model was first tested against existing literature analyses for the reference antenna to enable plasma diagnostics, and subsequently was used to analyze the antenna of interest. The fundamental limitations of transmission-line theory preclude quantitative comparison of resonance frequencies, especially at high frequencies. However, the theory does predict the low frequency, very-low attenuation sheath-wave propagation band above the cyclotron frequency as confirmed by the experimental observation of antenna resonances within that band. This band had not been observed before, so in practical terms it provides yet another channel for the propagation of EMI on space vehicles. The theoretical sheath wave passband and stopband behaviour is similar to experimental observations, which shows the utility of the transmission-line theory at low frequencies in spite of the crude approximations employed in its derivation. Admittance computations were used to explore plasma conditions characteristic of the ionospheric environment in which the OEDIPUS-C rocket experiment was carried out although comparable laboratory experiments were not done.

Future work should involve experiments with higher plasma magnetization which more appropriately corresponds to the conditions encountered by the OEDIPUS-C rocket. Moreover, experiments with antenna length variation would facilitate quantitative analysis of the sheath wave resonance behaviour.

Appendix

DERIVATION OF PLASMA FREQUENCY FROM EXPERIMENTS

The lowest resonance of a monopole in free space occurs at a frequency f_{ro} when the monopole length H is equal to a quarter wavelength, that is,

$$H = \frac{c}{4f_{ro}} \qquad \text{(A-1)}$$

In a cold, lossless, isotropic plasma of permittivity $\varepsilon_p = \varepsilon_0 K_0$, this resonance occurs at

$$H = \frac{c}{4f_r\sqrt{K_0}} \qquad \text{(A-2)}$$

Equating the right sides of the first and second equations gives

$$f_r = \frac{f_{ro}}{\sqrt{K_0}} \qquad \text{(A-3)}$$

To approximately account for the effect of the magnetic field, K_0 is replaced by K' for the field-parallel antenna. For a collisionless plasma,

$$K' = 1 - \frac{\left(\frac{f_p}{f}\right)^2}{1 - \left(\frac{f_c}{f}\right)^2} = \frac{f^2 - f_c^2 - f_p^2}{f^2 - f_c^2} \qquad \text{(A-4)}$$

Therefore, with $f = f_r$, eq. (A-3) can be re-written as

$$\frac{f_r^2(f_r^2 - f_c^2 - f_p^2)}{f_r^2 - f_c^2} = f_{ro}^2 \qquad \text{(A-5)}$$

Solving (A-5) for the plasma frequency yields

$$f_p^2 = -\left[\left(\frac{f_{ro}}{f_r}\right)^2 (f_r^2 - f_c^2) - f_r^2 + f_c^2\right] = (f_r^2 - f_c^2)\left[1 - \left(\frac{f_{ro}}{f_r}\right)^2\right] \qquad \text{(A-6)}$$

REFERENCES

[1] K. G. Balmain, "Plasma effects in EMC," in *Handbook of Electromagnetic Compatibility*, Chapter 26, pp. 963-980, 1995.

[2] J.-J. Laurin, "Study of sheath wave propagation in a magnetoplasma," M.A.Sc. thesis, University of Toronto, Toronto, 1986.

[3] D. A. Baker, "Transverse sheath wave propagation in a magnetoplasma," M.A.Sc. thesis, University of Toronto, Toronto, 1991.

[4] H. G. James and K. G. Balmain, "Space plasma experiments with the tethered OEDIPUS-C payload," *Proc. Fourth Int. Conf. on Tethers in Space*, NASA, Washington, D.C., 10-14 Apr. 1995.

[5] H. G. James, K. G. Balmain, C. C. Bantin, and G. W. Hulbert, "Sheath waves observed on OEDIPUS-A," *Radio Sci.*, vol. 30, no. 1, pp. 57-73, Jan.-Feb., 1995.

[6] K. G. Balmain, H. G. James, and C. C. Bantin, "Magnetoplasma sheath waves on a conducting tether in the ionosphere, with applications to EMI propagation on large space structures," *Proceedings of the Fourth Annual Workshop on Space Operations, Applications, and Research (SOAR '90)*, Albuquerque, NM, 26-28 June 1990, NASA Conference Publication 3103, pp. 646-654, published Feb. 1991.

[7] S. Adachi, T. Ishizone, and Y. Mushiake, "Transmission line theory of antenna impedance in a magnetoplasma," *Radio Sci.*, vol. 12, no. 1, pp. 23-31, Jan.-Feb., 1977.

[8] S. Miyazaki, "Radio frequency characteristic of electrode immersed in magnetoplasma and its application to plasma diagnostic techniques", *Journal of the Radio Research Laboratories*, vol. 15, no. 78, pp. 81-103, Mar. 1968.

[9] G. Morin, "Radio-frequency fields around conductors in plasma," Ph.D. dissertation, University of Toronto, Toronto, 1987.

[10] S. C. Brown, *Basic Data of Plasma Physics*, The MIT Press, Cambridge, Mass., 1959.

[11] P. C. Stangeby, Course notes from AER505S, *Plasma Physics and Fusion Energy*, 1995.

[12] R. E. Kiel, "Electrostatic probe theory for free molecular cylinders," *AIAA Journal*, vol. 6, no. 4, pp. 708-712, Apr. 1968.

[13] E. C. Jordan and K. G. Balmain, *Electromagnetic Waves and Radiating Systems*, Prentice-Hall, New Jersey, 1968.

[14] Y. Mushiake, "Electromagnetic Waves along an infinitely long and thin conducting wire in a magneto-ionic medium," *J. Res. Natl. Bur. Stand.*, *Sect. D*, 69(4), pp. 503-510, 1964.